



Neutron Star Mergers Might Not Be the Only Source of r -process Elements in the Milky Way

Benoit Côté^{1,2,3,17} , Marius Eichler⁴ , Almudena Arcones^{4,5}, Camilla J. Hansen⁶ , Paolo Simonetti⁷ , Anna Frebel^{3,8} ,
Chris L. Fryer^{3,9,10,11,12,17} , Marco Pignatari^{1,3,13,17} , Moritz Reichert⁴ , Krzysztof Belczynski¹⁴, and

Francesca Matteucci^{7,15,16} 

¹ Konkoly Observatory, Research Centre for Astronomy and Earth Sciences, Hungarian Academy of Sciences, Konkoly Thege Miklos ut 15-17, H-1121 Budapest, Hungary; benoit.cote@csfk.mta.hu

² National Superconducting Cyclotron Laboratory, Michigan State University, East Lansing, MI 48824, USA

³ Joint Institute for Nuclear Astrophysics—Center for the Evolution of the Elements, USA

⁴ Institut für Kernphysik, Technische Universität Darmstadt, Schlossgartenstr. 2, Darmstadt D-64289, Germany

⁵ GSI Helmholtzzentrum für Schwerionenforschung GmbH, Planckstr. 1, Darmstadt D-64291, Germany

⁶ Max Planck Institute for Astronomy, Königstuhl 17, D-69117 Heidelberg, Germany

⁷ Astronomy Department, University of Trieste, Via Tiepolo 11, I-34127 Trieste, Italy

⁸ Department of Physics and Kavli Institute for Astrophysics and Space Research, Massachusetts Institute of Technology, Cambridge, MA 02139, USA

⁹ Center for Theoretical Astrophysics, LANL, Los Alamos, NM 87545, USA

¹⁰ Department of Astronomy, The University of Arizona, Tucson, AZ 85721, USA

¹¹ Department of Physics and Astronomy, The University of New Mexico, Albuquerque, NM 87131, USA

¹² The George Washington University, Washington, DC 20052, USA

¹³ E.A. Milne Centre for Astrophysics, Department of Physics & Mathematics, University of Hull, HU6 7RX, UK

¹⁴ Nicolaus Copernicus Astronomical Center, Polish Academy of Sciences, ul. Bartycka 18, 00-716 Warsaw, Poland

¹⁵ I.N.A.F. Osservatorio Astronomico di Trieste, via G.B. Tiepolo 11, I-34131, Trieste, Italy

¹⁶ I.N.F.N. Sezione di Trieste, via Valerio 2, I-34134 Trieste, Italy

Received 2018 September 7; revised 2019 March 16; accepted 2019 March 17; published 2019 April 22

Abstract

Probing the origin of r -process elements in the universe represents a multidisciplinary challenge. We review the observational evidence that probes the properties of r -process sites, and address them using galactic chemical evolution simulations, binary population synthesis models, and nucleosynthesis calculations. Our motivation is to define which astrophysical sites have significantly contributed to the total mass of r -process elements present in our Galaxy. We found discrepancies with the neutron star (NS–NS) merger scenario. When we assume that they are the only site, the decreasing trend of [Eu/Fe] at [Fe/H] > -1 in the disk of the Milky Way cannot be reproduced while accounting for the delay-time distribution (DTD) of coalescence times ($\propto t^{-1}$) derived from short gamma-ray bursts (GRBs) and population synthesis models. Steeper DTD functions ($\propto t^{-1.5}$) or power laws combined with a strong burst of mergers before the onset of supernovae (SNe) Ia can reproduce the [Eu/Fe] trend, but this scenario is inconsistent with the similar fraction of short GRBs and SNe Ia occurring in early-type galaxies, and it reduces the probability of detecting GW170817 in an early-type galaxy. One solution is to assume an additional production site of Eu that would be active in the early universe, but would fade away with increasing metallicity. If this is correct, this additional site could be responsible for roughly 50% of the Eu production in the early universe before the onset of SNe Ia. Rare classes of supernovae could be this additional r -process source, but hydrodynamic simulations still need to ensure the conditions for a robust r -process pattern.

Key words: Galaxy: abundances – stars: abundances – nuclear reactions, nucleosynthesis, abundances – binaries: close

1. Introduction

Understanding the origin of rapid neutron-capture process (r -process) elements in the universe requires a multiscale framework including nuclear astrophysics, stellar spectroscopy, gravitational waves, short gamma-ray bursts (GRBs), and galaxy formation theories (e.g., Beers & Christlieb 2005; Arnould et al. 2007; Berger 2014; Frebel & Norris 2015; Fernández & Metzger 2016; Abbott et al. 2017b; Thielemann et al. 2017; Frebel 2018; Horowitz et al. 2018; Cowan et al. 2019). To best interpret stellar abundances of r -process elements¹⁸ derived from spectroscopy, nucleosynthesis calculations must be convolved with galaxy evolution simulations. To include r -process sites in such simulations, the general

properties of these sites must be known, which in the case of neutron star (NS–NS) mergers can be constrained by gravitational wave and short GRB detections.

The goal of our study is to build a coherent interdisciplinary picture to identify which astrophysical site(s) has (have) significantly contributed to the amount of r -process elements present in the Milky Way. We review the different observational evidence that probes the properties of r -process sites, and investigate them from the perspective of galactic chemical evolution (GCE) simulations, binary population synthesis models, and theoretical nucleosynthesis. In particular, we focus on the tensions that emerge when NS–NS mergers are assumed to be the only r -process site (see Table 1). We refer to Duggan et al. (2018) and A. Skúladóttir et al. (in preparation) for a discussion of r -process sites in dwarf galaxies.

Many studies addressed the challenge of explaining with NS–NS mergers the presence of Eu, a lanthanide element, in

¹⁷ NuGrid Collaboration, <http://nugridstars.org>.

¹⁸ By r -process elements we mean neutron-capture elements that are, to the best of our knowledge, mostly produced by the r -process.

Table 1List of Agreements and Inconsistencies when We Assume that Current Models of NS–NS Mergers and MR SNe Are the only r -process Site for Elements in between the Second and Third Peaks

Observational Constraints	NS–NS Mergers			MR SNe (Section 5.4)
	No DTD (Section 5.1)	t^{-1} DTD (Section 5.2)	Modified DTD (Section 5.3)	
Production of a robust main r -process pattern (Section 2.1.1)	Yes	Yes	Yes	Maybe
Possibility of producing actinides elements (Section 2.1.1)	Yes	Yes	Yes	Yes
Large scatter of [Eu/Fe] in metal-poor stars (Section 2.1.3)	Yes	Yes	Yes	Maybe
Stars with [Eu/Fe] > 0.3 at [Fe/H] \lesssim -2 (Figure 1)	Maybe	Maybe	Maybe	Yes
Decreasing trend of [Eu/Fe] at [Fe/H] > -1 (Section 2.2)	Yes	No	Yes	Yes
Fraction of short GRBs in early-type galaxies (Section 2.3)	No	Yes	No	...
LIGO/Virgo local NS–NS merger rate density (Section 2.4.2)	Yes	Yes	Yes	Maybe
Probability of detecting GW170817 in S0 galaxy (Section 2.4.1)	Zero	Low	Very low	...

Note. Three assumptions are made for the DTD function of NS–NS mergers: 1—follow the lifetime of massive stars with short constant delay times (without a DTD function), 2—DTD function in the form of t^{-1} , and 3—modified DTD functions, either a steeper $t^{-1.5}$ power law or a t^{-1} power law combined with a prompt burst of mergers before the onset of SNe Ia. For each observational constraint, a *Yes* or a *No* highlights whether the selected r -process site is consistent with the constraint. A *Maybe* means that the situation is unclear. We refer to Section 5.5 for a discussion of the possible contribution of multiple sites on the total budget of r -process elements in the Milky Way. This table reflects the current state of our understanding. Further observations and/or improved models could change the interpretation shown in this table.

the atmosphere of the most metal-poor stars ([Fe/H] \lesssim -2) of the Galactic halo (e.g., Argast et al. 2004; Matteucci et al. 2014; Cescutti et al. 2015; Ishimaru et al. 2015; Shen et al. 2015; Wehmeyer et al. 2015; Safarzadeh et al. 2018; Haynes & Kobayashi 2019, see also Section 5.5). In this paper, we instead focus on the decreasing trend of [Eu/Fe]¹⁹ at [Fe/H] > -1 in the Galactic disk. Currently, this trend cannot be well reproduced by invoking a proper delay-time distribution (DTD) for NS–NS mergers (Côté et al. 2017a; Hotokezaka et al. 2018; Simonetti et al. 2019). This distribution can be seen as the probability of a merger event to occur at a given delay time following the formation of the binary system.

In this paper, we explore different DTD functions for NS–NS mergers in order to recover the evolution of [Eu/Fe] in the Galactic disk using chemical evolution models. We then discuss whether these new DTD functions are consistent with other constraints outside the world of chemical evolution, such as the host galaxies of short GRBs, gravitational wave detections, and binary population synthesis predictions. We also present a list of alternative r -process enrichment scenarios in the Milky Way with multiple r -process sites involving rare classes of supernova, and discuss their implications with respect to a diverse range of observational and theoretical constraints. Overall, this work aims to isolate and highlight the current interdisciplinary tensions that need to be addressed in future studies in order to identify the dominant r -process site(s) in the Milky Way.

The outline of this paper is as follows. We review the observational evidence related to the production of r -process elements in Section 2. In Sections 3, 3.4, and 4, we address the properties of r -process sites from the point of view of GCE simulations, binary population synthesis models, and theoretical nucleosynthesis calculations, respectively. In Section 5 we highlight the interdisciplinary tensions associated with existing r -process enrichment scenarios involving compact binary mergers and magnetorotational (MR) supernovae, and propose alternative scenarios to be confirmed or disproved by

future work. Our discussion and conclusions are given in Sections 6 and 7, respectively.

2. Observational Evidence

Here we review the observational evidence that probes the properties of the r -process sites. We interpret these observables with numerical simulations in Sections 3 and 4, and attempt to build a consistent multidisciplinary picture in Section 5.

2.1. Neutron-capture Elements in Metal-poor Stars

Metal-poor stars in the Galactic halo and in dwarf galaxies can be unique tracers of r -process nucleosynthesis in the early universe (e.g., Sneden et al. 2008; Frebel 2018; Horowitz et al. 2018). Throughout this paper, we refer to the three peaks in the r -process abundance distribution, the first peak at Se–Kr, the second peak at Te–Xe, and the third peak at Os–Pt–Au. Heavier than the third peak are the actinide elements such as Th and U. We note that the residual pattern in the solar r -process is obtained by subtracting the contribution of the slow neutron-capture process (s -process) from the total solar abundances (e.g., Kappeler et al. 1989; Arlandini et al. 1999; Burris et al. 2000; Simmerer et al. 2004; Sneden et al. 2008; Bisterzo et al. 2014).

2.1.1. r -process Enhanced Stars

For stars with strong enhancements in neutron-capture elements, abundances of more than 35 elements between Sr and U can be derived (Roederer & Lawler 2012; Roederer et al. 2012b; Siqueira Mello et al. 2013; Mashonkina et al. 2014; Ji & Frebel 2018), typically with accuracies better than ± 0.2 dex, owing to large telescopes, high-resolution spectrographs, and improved knowledge of stellar parameters and atomic physics (e.g., Sneden et al. 2003; Hansen et al. 2015a; Ezzeddine et al. 2017). Some metal-poor stars are moderately or strongly enhanced in r -process elements and are classified based on their [Eu/Fe] and [Ba/Eu] ratios: r-I stars when [Eu/Fe] > 0.3 and [Ba/Eu] < 0, and r-II stars when [Eu/Fe] > 1.0 and [Ba/Eu] < 0. We note that Ba is actually past the second r -process

¹⁹ [A/B] \equiv $\log_{10}(n_A/n_B) - \log_{10}(n_A/n_B)_\odot$, where n_A and n_B represent the number density in the stellar atmosphere of elements A and B, respectively. The second term on the right-hand side represents the solar composition.

peak. Eu is located between the second and third r -process peak.

Sneden et al. (2003) first showed that the abundances of CS 22892-052, an r -II star, were similar within 0.2–0.3 dex to the solar r -process pattern between the second and third peak. Since then, many studies found additional r -process enhanced stars that also show this pattern with similar precisions (Roederer et al. 2009, 2012b; Cowan et al. 2011; Mashonkina et al. 2014; Ji et al. 2016b; Placco et al. 2017; Holmbeck et al. 2018; Sakari et al. 2018). This pattern has also been found in dwarf galaxy stars, such as in Reticulum II (Ji et al. 2016b; Ji & Frebel 2018). This universal abundance pattern, between the second and third r -process peak, is referred to as the main r -process. Deriving abundances for elements *in* the second r -process peak requires space telescopes with spectrographs operating in the ultraviolet. This has been done for only a handful of stars, and their abundances are consistent with the main portion of the scaled solar r -process pattern (Roederer & Lawler 2012; Roederer et al. 2012a).

While the main r -process observationally appears very robust, r -process enhanced stars do show large variations up to ~ 1 dex in first-peak neutron-capture elements such as Sr, Y, and Zr (e.g., Hansen et al. 2014, 2018b; Roederer et al. 2014a; Ji et al. 2016b; Ji & Frebel 2018; Spite et al. 2018). Although the origin of these variations is still unclear, it suggests that there is more than one astrophysical site that can produce the first-peak elements (e.g., Hansen et al. 2014; Cescutti et al. 2015; Spite et al. 2018). At low metallicity, these elements could be made by different nucleosynthesis processes (see, e.g., Montes et al. 2007; Roederer et al. 2010), such as neutrino-driven winds and the νp -process in CC SNe (Fröhlich et al. 2006; Farouqi et al. 2009; Roberts et al. 2010; Arcones & Montes 2011; Arcones & Thielemann 2013), the s -process in fast-rotating massive stars (Pignatari et al. 2008; Frischknecht et al. 2016), or the intermediate neutron-capture process (i -process, Roederer et al. 2016a).

In addition to variations in the first peak, a range of abundances is found in the actinide elements with atomic number $Z \geq 80$ (e.g., Hill et al. 2002; Roederer et al. 2009). Stars with a high Th/Eu ratio relative to the solar r -process pattern have been termed actinide-boost stars. Ji & Frebel (2018) recently reported the discovery of an actinide-deficient star in Reticulum II. This has broadened the range of Th abundances relative to the solar pattern to ~ 0.6 dex (see also Schatz et al. 2002; Roederer et al. 2009; Mashonkina et al. 2014; Hansen et al. 2018a; Holmbeck et al. 2018). We note that U abundances scale with Th values, but only very few U measurements are available. It is currently difficult to determine whether the variations in actinide abundances is a result of different r -process sites or is the trace of different ejecta with different physical conditions within the same site (see discussion in Section 6.4).

2.1.2. Limited r -process Stars

In contrast to the r -process enhanced stars, the majority of very metal-poor stars with $[\text{Fe}/\text{H}] < -2.0$ do not show any significant enhancements in neutron-capture elements. Although their abundances or upper limits in halo stars are often extremely low, they still show large star-to-star scatter. Some of these stars display no supersolar enhancement in neutron-capture elements but nevertheless display a systematic depletion of Ba and heavier elements relative to the abundances

of lighter neutron-capture elements such as Sr. Stars with this signature have recently been called limited r -process stars (Frebel 2018). The metal-poor star HD 122563 (Honda et al. 2006) is a famous example. However, as for the large scatter in the abundances of first-peak elements in r -process enhanced metal-poor stars (see Section 2.1.1), the nucleosynthetic origin (s) of limited r -process stars is still unclear.

2.1.3. Scatter of $[\text{Eu}/\text{Fe}]$ in Galactic Halo Stars

The large scatter seen in the $[\text{Eu}/\text{Fe}]$ ratio of r -process enhanced metal-poor stars in the Milky Way halo (blue crosses in Figure 1) compared to the smaller scatter seen in $[\alpha/\text{Fe}]$ ²⁰ indicates that the production of Eu in the early universe must have been rare and prolific compared to the production of α elements by standard CC SNe (e.g., Cescutti et al. 2015; Hirai et al. 2015; Wehmeyer et al. 2015; Naiman et al. 2018). The recent analysis of Macias & Ramirez-Ruiz (2018) suggests a minimum ejection of $\sim 10^{-3} M_{\odot}$ of r -process material per event to explain the most Eu-enhanced stars. The rarity of r -process events is also necessary to explain the low frequency of r -process enhanced ultra-faint dwarf galaxies such as Reticulum II (Ji et al. 2016a; Roederer et al. 2016b). A comparison between the abundance of ^{244}Pu in the Earth's ocean crust and the value derived for the early solar system also supports the idea that the r -process elements should be produced in rare events that eject a large amount of mass (Hotokezaka et al. 2015; Wallner et al. 2015; Lugaro et al. 2018).

2.2. Evolution of $[\text{Eu}/\text{Fe}]$ in the Galactic Disk

At higher metallicity ($[\text{Fe}/\text{H}] > -1.5$) in the Galactic disk, there is no star with a clean r -process signature because of the production of neutron-capture elements by the s -process (e.g., Gallino et al. 1998). To probe the evolution of r -process elements in disk stars, we use Eu. According to the solar r -process pattern, defined by subtracting the s -process pattern from the total solar abundance pattern, Eu was produced at $\sim 97\%$ by the r -process (e.g., Burris et al. 2000) at the time the solar system formed 4.6 Gyr ago (Connelly et al. 2017). We note, however, that there are uncertainties in s -process yields (e.g., Bisterzo et al. 2014; Cristallo et al. 2015), and that the i -process could potentially alter the exact composition of the r -process residuals by contributing to the production of neutron-capture elements (see, e.g., Dardelet et al. 2014; Hampel et al. 2016; Roederer et al. 2016a; Côté et al. 2018a; Denissenkov et al. 2018). We discuss the possible production of Eu by the i -process in Section 6.5. Throughout this paper, we assume that Eu is a reliable r -process tracer.

An important feature of the chemical evolution of Eu in the Milky Way is the decreasing trend of $[\text{Eu}/\text{Fe}]$ in the disk, as recorded in stars with $[\text{Fe}/\text{H}] > -1$ (cyan dots in Figure 1). These data behaves similar to the chemical evolution of $[\alpha/\text{Fe}]$ (see, e.g., Bensby et al. 2014; Buder et al. 2018; Spina et al. 2018). Because α elements are mostly produced in massive stars (e.g., Woosley et al. 2002; Nomoto et al. 2013), we can assume that the overall production rate of r -process elements also follows the lifetime of massive stars. In particular, because this decreasing trend originates from the additional production of Fe by SNe Ia that mixes with the material ejected by CC SNe (e.g., Matteucci & Greggio 1986; Matteucci et al.

²⁰ The α elements are mostly produced by massive stars and include elements such as O, Mg, Si, Ca, and Ti.

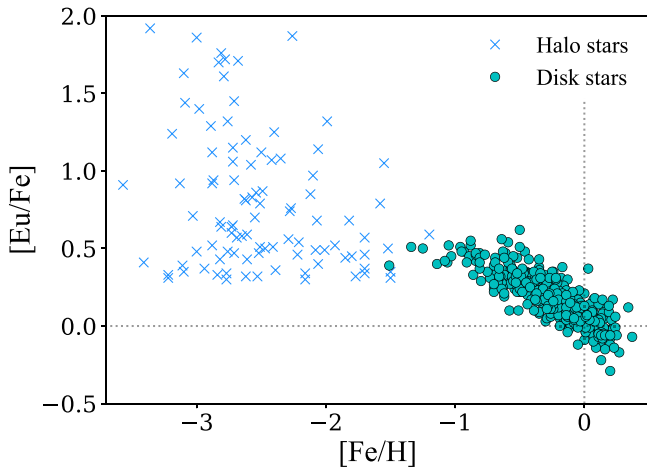


Figure 1. Evolution of europium abundances ($[\text{Eu}/\text{Fe}]$) as a function of iron abundances ($[\text{Fe}/\text{H}]$) observed in the Milky Way. The blue crosses represent a compilation of data extracted with the JINABase (Abolima & Frebel 2017), containing Burris et al. (2000), Sneden et al. (2003), Christlieb et al. (2004), Barklem et al. (2005), Frebel et al. (2007), Aoki et al. (2013), Roederer et al. (2014b), and Hansen et al. (2015b). We excluded upper limits and only selected stars with $[\text{Eu}/\text{Fe}] > 0.3$ and $[\text{Ba}/\text{Eu}] < 0$. The latter criterion aims to remove metal-poor s, i, and r+s stars. To this compilation, we added the 12 r-II stars found in Hansen et al. (2018b). The cyan circles are disk star data taken from Battistini & Bensby (2016). The dotted black lines mark the solar values (Asplund et al. 2009).

2009; Few et al. 2014), the production of r -process elements should occur on timescales shorter than SNe Ia, as for α elements (see Section 3 for more details). We note that the AMBRE Project recently measured abundances for Gd and Dy, two other tracer elements of the r -process, in the Galactic disk (Guiglion et al. 2018). They showed that $[\text{Gd}/\text{Fe}]$ and $[\text{Dy}/\text{Fe}]$ also have decreasing trends at $[\text{Fe}/\text{H}] > -1$.

2.3. Short GRBs and SNe Ia

While long-duration GRBs are associated with the explosion of massive stars, the progenitors of short-duration GRBs are believed to be NS–NS or black hole–neutron star (BH–NS) mergers (see Berger 2014 for a review). The detection of the short GRB that followed the NS–NS merger event GW170817 measured by LIGO/Virgo (Abbott et al. 2017b) reinforced this idea even more. We discuss the broad implication of GW170817 in Section 2.4. For now, we focus on the properties of short GRBs to probe the coalescence timescales of compact binary systems. We also compare results from short GRB observations with those of SNe Ia observations in order to investigate whether these two types of events occur on similar timescales. This is relevant for GCE simulations (see Section 3).

2.3.1. Host Galaxies

In the review of Berger (2014), $\sim 30\%$ of the 26 short GRBs with classified host galaxies are found in early-type galaxies (see also Fong et al. 2013; D’Avanzo 2015). A similar fraction of $\sim 1/3$ has been derived by Fong et al. (2017) with the 36 short GRBs detected between 2004 and 2017. Early-type (giant elliptical and S0) galaxies typically show a lack or low level of recent star formation compared to late-type (spiral) galaxies (e.g., González Delgado et al. 2016) and are dominated by old stellar populations (e.g., van de Sande et al. 2018). This implies that a certain fraction of NS–NS mergers, if they are the source

of short GRBs, must have long coalescence timescales. Otherwise, they would be exclusively found in star-forming late-type galaxies, as for core-collapse supernovae (CC SNe; e.g., Li et al. 2011) and long GRBs (e.g., Berger 2014).

A fraction of SNe Ia is also observed in early-type galaxies (e.g., Mannucci et al. 2005; Li et al. 2011). Using the ~ 370 classified SNe Ia found in the Lick Observatory Supernova Search, between 15% and 35% of SNe Ia occur in early-type galaxies (Figure 5 in Leaman et al. 2011, see also Graur et al. 2017a, 2017b), depending on whether we exclude or include S0-type galaxies in the early-type category. Similar percentages of 10% and 32% are obtained using the 103 SNe Ia with classified host galaxies from the Carnegie Supernova Project (Krisciunas et al. 2017). In a sample of ~ 450 classified SNe Ia found in the Sloan Digital Sky Survey-II (SDSS-II) Supernova Survey²¹ (Sako et al. 2014), between 12% and 40% of SNe Ia are found in galaxies with stellar masses above $(0.5\text{--}1.0) \times 10^{11} M_{\odot}$ (see also Uddin et al. 2017), which is roughly the mass range above which early-type galaxies become the dominant type in galaxy populations (e.g., Kelvin et al. 2014; Moffett et al. 2016; Thanjavur et al. 2016). Using the same sample, we find that $\sim 25\%$ of SNe Ia occur in passive galaxies that do not form stars anymore.

Compared to the $\sim 30\%$ derived for short GRBs with classified host galaxies, this suggests that short GRBs and SNe Ia occur on average on similar timescales.

2.3.2. Delay-time Distributions

The DTD function of an astronomical event represents the probability of that event to occur at a given time t following the formation of its progenitor objects. Different approaches for deriving observationally the DTD function of SNe Ia are described in Maoz et al. (2014). Regardless of the different methodologies, most studies point toward a DTD in the form of t^{-1} (Totani et al. 2008; Maoz et al. 2010, 2012; Graur et al. 2011, 2014; Perrett et al. 2012), which is consistent with the predictions of population synthesis models (e.g., Ruiter et al. 2009).

Similar techniques can be applied to short GRBs. According to Fong et al. (2017), and references therein, the DTD function of short GRBs could also be in the form of t^{-1} . This is also in agreement with population synthesis studies (e.g., Dominik et al. 2012; Chruslinska et al. 2018). As mentioned in Section 2.3.1, the statistics of short GRB detections is still low and the derived DTD function could change in the near future (see also discussion in Fong et al. 2017). We note that D’Avanzo (2015) argued for a steeper DTD function in the form of $t^{-1.5}$ for short GRBs. However, this provides tension with respect to the similar fraction of short GRBs and SNe Ia occurring in different types of galaxies (see Section 2.3.1), unless the DTD function of SNe Ia also turns out to be in the form of $t^{-1.5}$, as suggested by the recent analysis of Heringer et al. (2017).

Of the 13 confirmed NS–NS binary systems observed in the Milky Way compiled by Tauris et al. (2017), 6 have an estimated coalescence time. This excludes systems that will merge in more than 50 Gyr. The additional NS–NS binary PSR J1946+2052 discovered by Stovall et al. (2018) has an estimated coalescence time of 46 Myr. When sorted in an increasing order, these 7 NS–NS binaries should merge in 46,

²¹ <https://data.sdss.org/sas/dr10/boss/papers/supernova/>

86, 217, 301, 480, 1660, and 2730 Myr. Although a larger sample is needed to derive a reliable DTD function, the fact that 2 of the 7 systems have coalescence timescales longer than 1 Gyr is consistent with the idea that the number of NS–NS mergers, if they are responsible for short GRBs, should be distributed following a long-lasting DTD function.

2.4. The Gravitational Wave GW170817

The detection of GW170817 by LIGO/Virgo (Abbott et al. 2017b) and its associated electromagnetic emissions is the best direct evidence to date that NS–NS mergers can synthesize r -process elements. In the next subsections, we review the implication of this event on the contribution of NS–NS mergers on the origin of r -process elements in the Milky Way.

2.4.1. The Host Galaxy NGC 4993

This first NS–NS merger detection occurred in NGC 4993, an early-type galaxy (Abbott et al. 2017d; Coulter et al. 2017). Analysis of the properties of this galaxy revealed a current stellar mass of about $(0.3\text{--}1.4) \times 10^{11} M_{\odot}$ and a star formation rate (if any) below $\sim 10^{-2} M_{\odot} \text{ yr}^{-1}$ (Blanchard et al. 2017; Im et al. 2017; Levan et al. 2017; Pan et al. 2017), which is significantly lower than what is observed in late-type galaxies with similar stellar masses (see Figure 4 in González Delgado et al. 2016). According to Levan et al. (2017), an upper limit of only $\sim 1\%$ of the stellar mass could originate from young stars. Given the properties of the host galaxy of GW170817, Pan et al. (2017) argued that the delay between the formation of the progenitor binary system and the NS–NS merger event has likely been greater than ~ 3 Gyr. By convolving the star formation history of NGC 4993 with a DTD function in the form of t^{-1} , Blanchard et al. (2017) calculated the probability of the merger timescale to be between 6.8 and 13.6 Gyr, with 90% confidence.

According to population synthesis models, the DTD function of NS–NS mergers does extend up to ~ 10 Gyr, but most of the merger events are likely to occur within the first Gyr following the formation of the progenitor stars (e.g., Chruslinska et al. 2018). Therefore, according to Belczynski et al. (2017a), detecting the first NS–NS merger event in an early-type galaxy was unlikely, although not impossible. The low probability of this event is also discussed in Levan et al. (2017). With only one NS–NS gravitational wave detection, conclusions are limited, but the host galaxy of GW170817 does inform us that it is at least possible for NS–NS mergers to have gigayear-long coalescence timescales. We refer to Palmese et al. (2017) for a discussion of a possible formation mechanism for the binary neutron star system that led to GW170817 in NGC 4993.

2.4.2. The Kilonova AT 2017gfo (SSS17a)

The ultraviolet, optical, and infrared emission from GW170817 suggest a significant production of r -process elements (e.g., Chornock et al. 2017; Cowperthwaite et al. 2017; Drout et al. 2017; Pian et al. 2017; Tanaka et al. 2017; Villar et al. 2017). In particular, its late-time infrared emission suggests the production of lanthanide elements (e.g., Barnes & Kasen 2013; Fernández & Metzger 2016; Tanvir et al. 2017; Wollaeger et al. 2018, but see Rosswog et al. 2018; Wanajo 2018; Wu et al. 2018). Multidimensional simulations are based on two-component models (e.g., Tanvir et al. 2017). The first component is the neutron-rich dynamical ejecta that

produces heavy r -process elements up to the third peak at the time the compact objects collide. The second one is a wind component primarily composed of first-peak r -process elements, which is launched at later time after the compact objects have merged. We refer to Appendix C.1 for more details on these two components and on their nucleosynthesis.

All models, however, used approximate opacities because detailed databases of opacities for all heavy elements are not yet available. State-of-the-art studies used a few opacities as surrogates for the entire rare-Earth lanthanide element distribution (Barnes & Kasen 2013; Wollaeger et al. 2018), but many others used constant opacities as a function of temperature, density, and wavelength. In some calculations, the inferred ejected mass of heavy r -process elements is lower than $10^{-5} M_{\odot}$ (Arcavi et al. 2017). Most models predicted $\sim 0.001\text{--}0.01 M_{\odot}$ of dynamical ejecta and $\sim 0.01\text{--}0.03 M_{\odot}$ of wind ejecta, however (see Table 1 in Côté et al. 2018b).

The ejected mass of the dynamical and wind components depends on the total mass and the mass ratio of the merging neutron stars. Typically, systems with extreme mass ratios eject more dynamical mass (Korobkin et al. 2012; Bovard et al. 2017, and references therein) and produce higher disk masses (Giacomazzo et al. 2013). If the wind ejecta represent a constant fraction of the disk mass, we would expect the wind ejecta to also increase with more extreme mass ratios, although the exact amount of ejected mass depends on the simulation (see Siegel & Metzger 2018, and references therein). The current constraint on the neutron star mass ratio for GW170817 ranges from 0.4 to 1.0 (Abbott et al. 2017c).

Although the wind ejecta are thought to be mostly composed of first-peak r -process elements, they may also include some heavier elements. This could alter the ratio of the abundances between the second and third r -process peaks, an undesired effect given the robustness of the r -process between the second and third peaks, as observed in r -process enhanced metal-poor stars (see Section 2.1.1).

2.4.3. The Merger Rate Density

The local NS–NS merger rate density of $1540_{-1220}^{+3200} \text{ Gpc}^{-3} \text{ yr}^{-1}$ provided by LIGO/Virgo (Abbott et al. 2017c) represents a significant step forward in constraining the role of NS–NS mergers on the production of r -process elements in the universe. Several analytical calculations, based on estimates for the total mass of r -process elements currently present in the Milky Way, showed that the rate could be high enough to explain all the r -process mass with NS–NS mergers alone (Abbott et al. 2017a; Chornock et al. 2017; Cowperthwaite et al. 2017; Gompertz et al. 2017; Kasen et al. 2017; Rosswog et al. 2017b; Tanaka et al. 2017; Wang et al. 2017; Hotokezaka et al. 2018, see also Rosswog et al. 1999). A similar conclusion was derived using a compilation of GCE simulations (Côté et al. 2018b).

Unfortunately, the uncertainties in the merger rate and in the total mass ejected per NS–NS merger (see Section 2.4.2) remain very large, and it is not possible at the moment to come to a firm conclusion regarding the actual contribution of NS–NS mergers (see Figure 3 in Côté et al. 2018b). Therefore, although NS–NS mergers are likely to be an important site of r -process nucleosynthesis, their existence does not rule out possible contributions by other r -process sites, such as rare classes of CC SNe and BH–NS mergers.

3. Chemical Evolution Simulations

GCE simulations can bridge nuclear astrophysics efforts and stellar abundances derived from spectroscopy. In addition to the yields and properties of different enrichment sites, GCE simulations also take into account galaxy evolution processes such as star formation and interactions between galaxies and their surrounding medium (e.g., Gibson et al. 2003; Prantzos 2008; Nomoto et al. 2013; Matteucci 2014; Somerville & Davé 2015). In this section, we describe how GCE simulations can be used to test the impact of NS–NS mergers on the evolution of r -process elements in the Milky Way. The goal is not to use GCE simulations to define the dominant r -process site. The goal is rather to use these simulations to provide a constraint that must be combined with other constraints coming from the other fields of research covered in this paper.

Two approaches are commonly used to include NS–NS mergers in GCE simulations. The first is to assume that all NS–NS mergers occur after a constant delay time following the formation of the NS–NS binaries (e.g., Argast et al. 2004; Matteucci et al. 2014). The second approach is to assume that NS–NS mergers in a given stellar population are distributed in time according to a long-lasting DTD function typically in the form of t^{-1} (e.g., Shen et al. 2015; van de Voort et al. 2015). In the later approach, NS–NS mergers can have a wide range of coalescence times, from a few tens of megayears to several gigayears (e.g., Rosswog 2015). We explore alternative forms of DTD functions in Section 5.3.

3.1. Reproducing the Decreasing Trend of $[Eu/Fe]$

The bottom panel of Figure 2 shows the predicted evolution of $[Eu/Fe]$ as a function of galactic age assuming a constant delay time (black solid line) and a long-lasting DTD function ($\propto t^{-1}$, black dashed line) for NS–NS mergers, assuming they are the only source of Eu. These predictions come from a simplified version of the one-zone chemical evolution code OMEGA (Côté et al. 2017b). We adopted a constant star formation rate as a function of time and a closed-box environment, implying no gas exchange between the galaxy and its surrounding environment. This simplification, although not realistic, was adopted to facilitate the understanding of the decreasing trend of $[Eu/Fe]$ in a GCE context. The top panel of Figure 2 shows the production rate of Fe by CC SNe (blue solid line) and SNe Ia (red solid line), and the production rate of Eu by NS–NS mergers (black solid and dashed lines), following the two approaches described above. The interpretation of the residual pink dashed line is discussed in Section 5.5.

In this simplified framework, because massive stars only live for a few tens of Myr, the Fe production reaches an equilibrium after ~ 40 Myr. The production of Fe by SNe Ia does not show this equilibrium because SNe Ia have a wide range of delay times that span from ~ 100 Myr to more than ~ 10 Gyr (e.g., Ruiters et al. 2009). This means that the first stellar population formed at the beginning of the simulation will still produce SNe Ia after ~ 10 Gyr, which is roughly the lifetime of the simulated galaxy.

When we assume that NS–NS mergers follow the lifetime of massive stars, the production rate of Eu also reaches an equilibrium before the onset of SNe Ia (black solid line in top panel of Figure 2). Under this assumption, when SNe Ia start to appear at ~ 100 Myr, the $[Eu/Fe]$ ratio will bend and start to decrease as a function of time (black solid line in the bottom

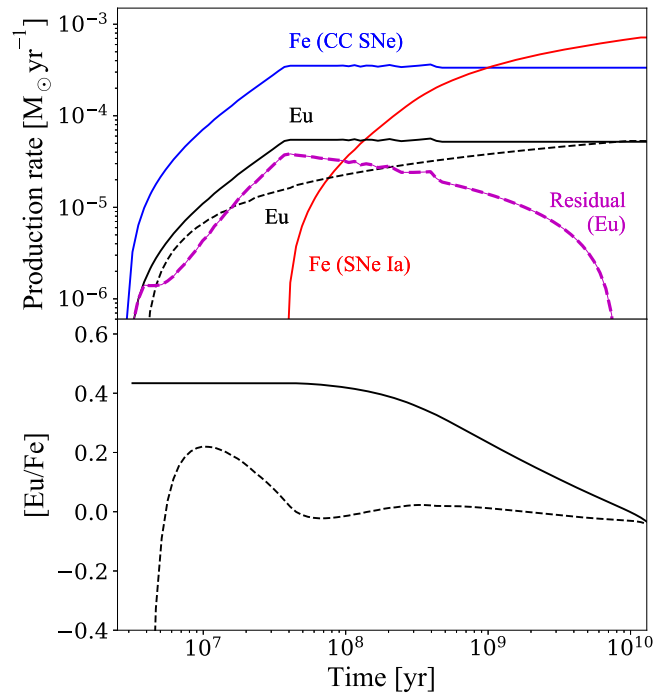


Figure 2. Depiction of how the decreasing trend of $[Eu/Fe]$ can be generated with time. Top panel: production rates of Fe in CC SNe (blue line) and SNe Ia (red line) as a function of time in a galaxy with a constant star formation rate of $1 M_{\odot} \text{ yr}^{-1}$. The black lines show the hypothetical production rate of Eu (scaled up by a factor of 4×10^5 for visualization purposes) when assuming that Eu is ejected following the lifetime of massive stars (solid black line) or a delay-time distribution function in the form of t^{-1} (dashed black line), similar to one adopted for SNe Ia. The pink residual dashed line is a possible additional source of Eu in the early universe (discussed in Section 5.5), obtained by subtracting the black dashed line from the solid black line. Bottom panel: evolution of $[Eu/Fe]$ using the two different assumptions used in the top panel for the production timescale of Eu (same line styles). Results have been calculated with a simplified version of OMEGA (see Section 3.1), assuming $3.35 \times 10^{-4} M_{\odot}$ of ejected Fe for each unit of stellar mass formed for CC SNe (see Côté et al. 2017a), $0.7 M_{\odot}$ of ejected Fe per SN Ia, and $10^{-5} M_{\odot}$ of ejected Eu per r -process event.

panel of Figure 2). Indeed, while the production rate of Eu is in equilibrium, the production rate of Fe increases, thus progressively reducing the $[Eu/Fe]$ ratio.

On the other hand, when we use a long-lasting DTD function in the form of t^{-1} , the production rate of Eu no longer reaches an equilibrium (black dashed line in top panel of Figure 2). In fact, because the adopted DTD function of SNe Ia is also in the form of t^{-1} (see Section 2.3), the production rates of Eu and Fe evolve in a similar way when SNe Ia start to contribute. This results in a nearly constant value for $[Eu/Fe]$ beyond ~ 100 Myr (black dashed line in the bottom panel of Figure 2). This flat trend, however, is not consistent with the decreasing trend observed in the Galactic disk (see Figure 1).

3.2. Common Message Sent by Different Studies

The inability of reproducing the decreasing trend of $[Eu/Fe]$ in the Galactic disk using NS–NS mergers with a DTD function of the form of t^{-1} is independent of the complexity of the GCE simulations. Indeed, when we assume constant delay times for NS–NS mergers, all Milky Way simulations reproduce the decreasing trend of $[Eu/Fe]$ (Argast et al. 2004; Matteucci et al. 2014; Cescutti et al. 2015; Wehmeyer et al. 2015; Côté et al. 2017a). On the other hand, when we assume a DTD function in the form of t^{-1} , all GCE simulations fail to match the

decreasing trend of $[\text{Eu}/\text{Fe}]$ for $-1 < [\text{Fe}/\text{H}] < 0$ (Shen et al. 2015; van de Voort et al. 2015; Komiya & Shigeyama 2016; Côté et al. 2017a; Hotokezaka et al. 2018; Naiman et al. 2018). The latter studies represent a wide variety of GCE approaches including simple one-zone models, semianalytic models of galaxy formation, and cosmological hydrodynamic zoom-in simulations.

When assuming that all NS–NS mergers occur within 100 Myr following the formation of the massive star progenitors, Matteucci et al. (2014), Cescutti et al. (2015), and Côté et al. (2017a) showed that GCE predictions at $[\text{Fe}/\text{H}] > -1$ are unaffected by the choice of delay time (see also the blue lines in Figure 9 of Appendix A). However, when we use a long-lasting DTD function in the form of t^{-1} , our predictions at $[\text{Fe}/\text{H}] > -1$ become affected by the choice of the minimum delay time (see black lines in Figure 9). As described in Appendix A, however, even with a minimum delay time of 1 Myr, our GCE predictions cannot reproduce the decreasing trend of $[\text{Eu}/\text{Fe}]$ when we use the DTD function.

To summarize, in order to recover the decreasing trend of $[\text{Eu}/\text{Fe}]$, it seems not sufficient to make NS–NS mergers appear before SNe Ia, they also need to reach an equilibrium in the production of Eu. Because $[\text{Eu}/\text{Fe}]$ and $[\alpha/\text{Fe}]$ both start to decrease at $[\text{Fe}/\text{H}] \sim -1$, this equilibrium must be reached within the first few hundred Myr. Although in this section we assumed NS–NS mergers to be the only r -process site, the equilibrium requirement would be the same for any other site. It can also be applied in the context of multiple r -process sites (see Section 5.5). We refer to Hotokezaka et al. (2018) for a discussion on the impact of the minimum delay time of SNe Ia, as it could help generating a decreasing trend if that minimum delay time is set to 400 Myr or 1 Gyr.

3.3. Confirmation from Our Study

To support the conclusion made in Section 3.2, we tested the t^{-1} DTD function using the benchmark Milky Way model of Matteucci et al. (2014), which is based on the two-infall model originally described in Chiappini et al. (1997). We refer to Simonetti et al. (2019) for more details on this new implementation. In this multizone framework, which relaxes the instantaneous recycling approximation, the halo and thick disk form on a relatively short timescale (1–2 Gyr) by accretion of primordial gas. This represents the first-infall event, while the thin disk forms on a much longer timescale by means of a second independent episode of gas accretion. The thin disk is assumed to form inside-out with a timescale of 7 Gyr for the solar neighborhood. In this work, we only focus on the thin disk.

The model predicts at all times the gas fraction and its chemical composition. It takes into account the enrichment from stars of all masses ending their lives as white dwarfs and SNe of all types (II, Ia, Ib, and Ic), in addition to the nucleosynthesis occurring in novae and compact binary mergers. The adopted yields are taken from Karakas (2010) and Doherty et al. (2014a, 2014b) for asymptotic giant branch (AGB) and super-AGB stars, from Nomoto et al. (2013) for massive stars, from Iwamoto et al. (1999) for SNe Ia, from José & Hernanz (1998) for novae, and from Korobkin et al. (2012) for NS–NS mergers. The SN Ia rate is computed following the formalism of Greggio (2005). The rate of NS–NS mergers is calculated by convolving its DTD function with the star formation history of the Milky Way, which is generated

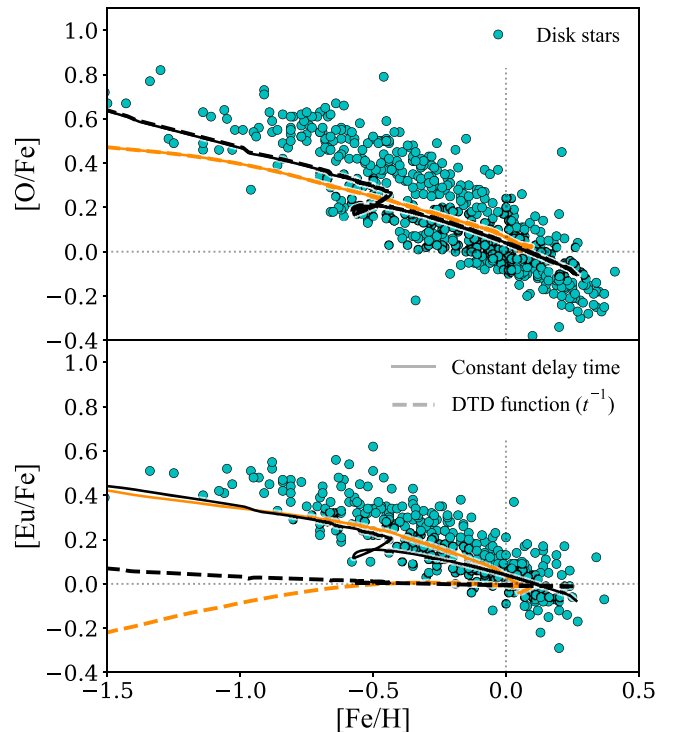


Figure 3. Predicted evolution of oxygen ($[\text{O}/\text{Fe}]$) and europium ($[\text{Eu}/\text{Fe}]$) abundances as a function of iron abundances ($[\text{Fe}/\text{H}]$) in the Galactic disk, using NS–NS mergers and the chemical evolution model of Côté et al. (2017b; OMEGA, orange lines) and Matteucci et al. (2014; black lines, see Section 3.3). The solid line shows the predictions when we assume that NS–NS mergers all occur after a constant delay time of 1 Myr following the formation of the binary systems, while the dashed line shows the predictions when we assume a delay-time distribution function in the form of t^{-1} to distribute NS–NS mergers as a function of time. Data derived from spectroscopy (cyan dots) are from Bensby et al. (2014) for $[\text{O}/\text{Fe}]$ and from Battistini & Bensby (2016) for $[\text{Eu}/\text{Fe}]$. The dotted black lines mark the solar values (Asplund et al. 2009).

following a Kennicutt–Schmidt law with a threshold in the gas surface density (Kennicutt 1998). The fraction of NS–NS binaries that eventually merge has been tuned to reproduce the current rate derived in Abbott et al. (2017b).

The bottom panel of Figure 3 shows the predictions of this model when a constant delay time (black solid line) and a t^{-1} DTD function (black dashed line) are used to calculate the rate of NS–NS mergers. As in previous studies (see Section 3.2), the long-lasting DTD function generates a flat trend for $[\text{Eu}/\text{Fe}]$ and does not reproduce the decreasing trend of the Galactic disk (cyan dots). The little loop at $[\text{Fe}/\text{H}] \sim -0.5$ is caused by the second-infall episode that introduces primordial gas in the galaxy that momentarily dilutes the Fe concentration relative to H. The top panel Figure 3 shows the evolution of $[\text{O}/\text{Fe}]$ as a comparison baseline for the decreasing trend of $[\text{Eu}/\text{Fe}]$.

Throughout this study, we also use the GCE code OMEGA (Côté et al. 2017b) in order to explore different DTD functions for NS–NS mergers (see Section 5.3), and to compare with the results of the GCE code of Matteucci et al. (2014; see orange lines in Figure 3). It consists of a classical one-zone model that adopts homogeneous mixing but relaxes the instantaneous recycling approximation. SNe Ia are distributed in time following a DTD function in the form of t^{-1} that is multiplied by the fraction of white dwarfs (see Côté et al. 2016 and Ritter et al. 2018a for more details.) Yields for low- and intermediate-mass stars, massive stars, SNe Ia, and NS–NS mergers are taken from Ritter et al. (2018b), Nomoto et al. (2013), Iwamoto

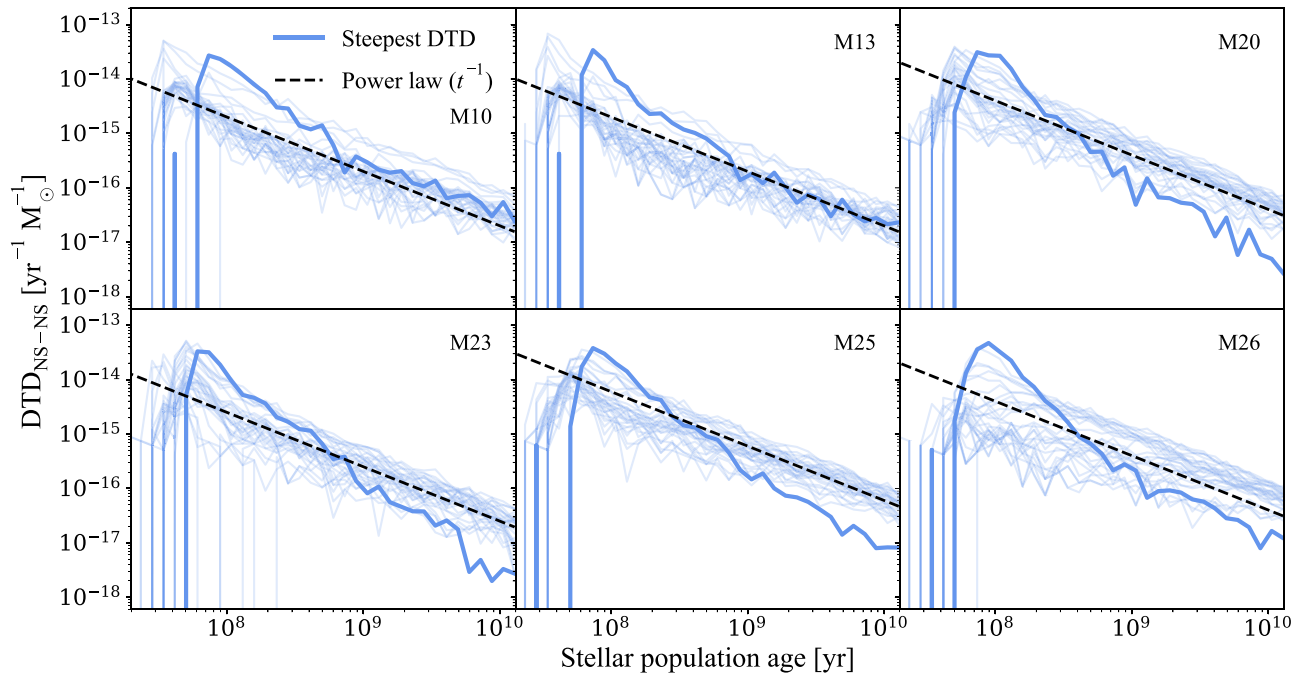


Figure 4. Delay-time distribution (DTD) functions of NS–NS mergers predicted by the population synthesis models described in Section 3.4 for a stellar population normalized to $1 M_{\odot}$. Each panel represents a different set of assumptions regarding the evolution of binary systems. The thin blue lines show the predictions for 32 different initial metallicities. The thick blue line shows the prediction with the steepest slope (to be used as an argument in Section 5.3). As a reference, the dashed black line shows a power-law DTD in the form of t^{-1} .

et al. (1999), and Arnould et al. (2007), respectively. In this paper, every OMEGA simulations have the same physical setup, only the delay time assumptions of NS–NS mergers are changed. By the end of all OMEGA simulations, the mass of gas within our Milky Way model is $9.5 \times 10^9 M_{\odot}$, the star formation efficiency is $2.9 \times 10^{-10} \text{ yr}^{-1}$, and the star formation rate is $2 M_{\odot} \text{ yr}^{-1}$.

3.4. Population Synthesis Models

Population synthesis models aim to follow the evolution of binary systems involving stars and compact remnants (white dwarfs, neutron stars, and black holes). The predictions of these models are typically for individual stellar populations where all stars are assumed to form at the same time with the same initial metallicity. In the context of this paper, these models are important because they predict the DTD functions of NS–NS and BH–NS mergers, which are crucial inputs for GCE simulations.

For this study, we use the previously calculated models M10, M13, M20, M23, M25, and M26 (see Belczynski et al. 2017b) that were obtained with the upgraded population synthesis code *StarTrack* (Belczynski et al. 2002, 2008). These six models aim to provide a range of solutions for the predicted DTD functions that reflects uncertainties in the evolution of binary systems. A short description of the *StarTrack* code and the models is included in Appendix B.

Figure 4 shows the DTD functions predicted by *StarTrack* for NS–NS mergers. For each model (each panel), the predictions at different metallicities are overall consistent with a simple power law in the form of t^{-1} . There are, however, interesting cases showing steeper power-law indexes (thick blue line) that are explored in Section 5.3. These results are consistent with other population synthesis studies (Chruslinska

et al. 2018; Giacobbo & Mapelli 2018; Kruckow et al. 2018; Vigna-Gómez et al. 2018).

An important physical ingredient driving the slope of the DTD function of NS–NS mergers is the distribution of orbital separations (a) of massive stars in binary systems (e.g., Tauris et al. 2017). According to Belczynski et al. (2018b), an orbital separation distribution in the form of a^{-1} tends to generate NS–NS merger DTD functions in the form of t^{-1} , while a distribution in the form of a^{-3} tends to generate steeper NS–NS merger DTD functions in the form of $t^{-1.5}$ (see also Figure 2 in Belczynski et al. 2018a).

Figure 5 shows the predictions for BH–NS mergers for the three models that generated the highest number of BH–NS mergers. Relative to NS–NS mergers, BH–NS mergers can appear earlier during the lifetime of a stellar population. As described in Section 3.2, however, this fact alone is unlikely to help generating a decreasing trend for [Eu/Fe] in chemical evolution simulations. The shape of their DTD functions is less in agreement with a power law in the form of t^{-1} , as there is typically a bump in between 0.1 and 1 Gyr. Compared to a t^{-1} power law, this implies a flatter power law before 1 Gyr followed by a steeper power law after 1 Gyr, at least for the M20 and M26 models.

4. R-process Nucleosynthesis Calculations

Here we discuss the connections of the GCE results above to theoretical r -process calculations. We give a more detailed review of the nucleosynthesis of r -process elements in different types of environments in Appendix C. R -process nucleosynthesis calculations are usually based on hydrodynamic simulations of scenarios that can provide very neutron-rich conditions. The most promising of these are currently compact binary mergers and MR supernovae, a rare class of CC SNe. Other possible scenarios include magnetized winds from proto-

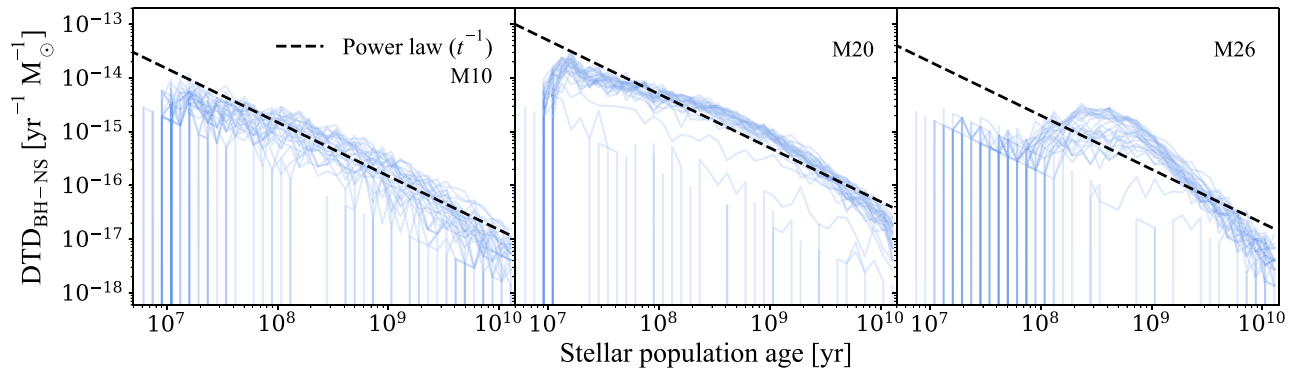


Figure 5. Same as in Figure 4, but for BH–NS mergers. Predictions showing vertical drops and discontinuities did not have sufficient BH–NS mergers to generate a statistically meaningful DTD function. Only the M10, M20, and M26 models are shown because the others did not predict enough BH–NS mergers to generate conclusive DTD functions.

neutron stars (Thompson 2003; Metzger et al. 2007, 2008; Vlasov et al. 2014; Thompson & ud-Doula 2018), pressure-driven outflows (Fryer et al. 2006), accretion disk winds from collapsars (Siegel et al. 2018), and the jets generated by a neutron star that accretes matter from its giant companion star (Papish et al. 2015; Soker & Gilkis 2017; Grichener & Soker 2018).

The evolution of the ejected mass depends on the evolution of density and temperature as a function of time, and on the initial electron fraction (Y_e). The latter serves as a measurement of the neutron fraction in the environment as it is defined as the proton-to-baryon ratio, $Y_e = Y_p / (Y_p + Y_n)$. If the Y_e is low ($Y_e \lesssim 0.25$), the neutron fraction (Y_n) will be high, and more neutrons will be available to be captured by seed nuclei, i.e., the neutron-to-seed ratio (Y_n/Y_{seed}) is high. Typically, the Y_e value is taken when the temperature drops below ~ 10 GK. The evolution of density and temperature is often categorized by the entropy and the expansion timescale of the ejecta, which are used as nucleosynthesis parameters.

4.1. Robustness of the Main r -process

An individual simulation of an environment can provide very different conditions for the ejecta. When several simulations are considered, the variations are even larger. For example, with NS–NS mergers, different possibilities can be studied by varying the masses of both neutron stars, the equation of state, and other input physics. We say that the r -process nucleosynthesis is robust when the relative abundance pattern is insensitive to such variations and is always similar between the second and third r -process peak. If the initial neutron-to-seed ratio is high enough ($Y_n/Y_{seed} > 150$), the r -process path runs into isotopes that are prone to fission, producing two (or more) fission fragments that can in turn continue to capture neutrons. This so-called “fission cycling” guarantees that the final yields produce a robust and reproducible abundance pattern independently of the exact hydrodynamical conditions (Beun et al. 2006; Goriely et al. 2011; Roberts et al. 2011; Korobkin et al. 2012; Rosswog et al. 2013; Eichler et al. 2015; Mendoza-Temis et al. 2015).

4.2. Neutron Star Mergers versus Supernovae

Because the uncertainties in nuclear properties and reaction rates involved in the r -process are still very large, model compositions for ejecta of different r -process sites should be considered qualitative predictions rather than precise results.

Nevertheless, some key differences can be expected in the final abundance patterns of NS–NS mergers and MR SNe if the conditions in the ejecta are reasonably different.

Hydrodynamic simulations suggest that the dynamical ejecta of NS–NS mergers are generally more neutron-rich than those of MR SNe, even if the entropy range is similar. This directly translates into higher initial neutron-to-seed ratios, and as a consequence, into a larger fraction of the ejecta where the third peak and the actinides region can be reached. While a large fraction of NS–NS merger ejecta coproduce the second and third r -process peaks, MR SN ejecta contain regions where the neutron-to-seed ratio is not high enough to produce third-peak elements, leading to the build-up of a distinct second r -process peak. As a result, the abundance ratio between the third and second peak for the total ejecta should be larger in dynamical ejecta of NS–NS mergers than in MR SNe. Varying contributions from disk and neutrino-driven wind ejecta in NS–NS mergers could unfortunately wash out this distinction.

Another observable could be the shape of the second peak itself. As described above, in MR SN ejecta, the predominant contribution in the build-up of the second peak comes from regions with moderate Y_e where the r -process flow is stopped at the shell closure at $N = 82$. In this case, the final shape of the second peak is mostly determined by β -decays and β -delayed neutron emissions. On the other hand, the neutron-rich NS–NS merger ejecta can produce a considerable amount of actinides with fission (and α -decay) on timescales that are similar to or longer than the r -process duration. Most nuclear mass models predict the majority of fissioning nuclei in the mass range $240 < A < 280$, which leads to fission fragments at or around the second peak. The production of fission fragments after the end of the r -process implies that the second peak in this case is shaped by the fission fragment distribution and their subsequent β -decays on top of the abundances that are already present at the time of r -process freeze-out.²²

To illustrate this, we have performed r -process calculations based on the NS–NS merger simulation of Rosswog et al. (2013), involving two neutron stars of $1.4 M_{\odot}$ each, and based on the MR SN model of Winteler et al. (2012; see Figure 6). Both sets of calculations were performed with fully enabled fission reactions (blue and red solid lines), as well as with a modified setup disabling fission from the moment when

²² Freeze-out is defined as the moment when the neutrons are almost exhausted and thus $Y_n/Y_{seed} \leq 1$. This coincides with time when β -decays become faster than neutron captures and can be identified with the corresponding timescales: $\tau_{\beta} < \tau_{(n,\gamma)}$.

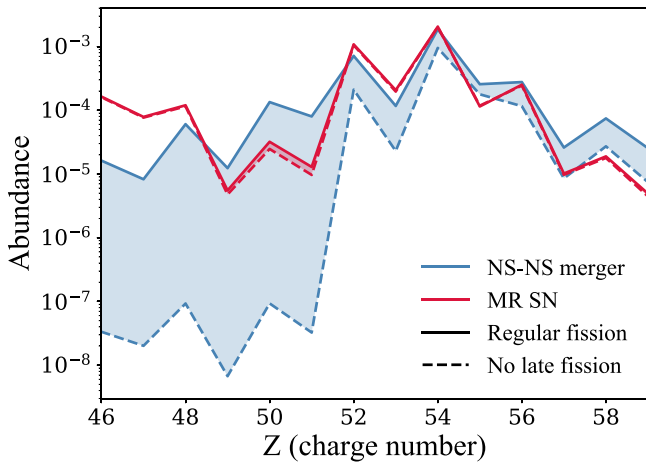


Figure 6. Predicted abundances of the second r -process peak for a neutron star (NS–NS) merger calculation (blue) and a magnetorotational supernova (MR SN) scenario (red), assuming either a continuous fission fragment production (“regular fission”) or a setup where fission fragment production is disabled after the r -process freeze-out (“no late fission”). The shaded regions represent the fission contribution to the final abundances of the second peak.

$Y_n/Y_{\text{seed}} \leq 1$ onward. The dashed lines in Figure 6 represent the β -decayed second peak material that is already present at the r -process freeze-out without any later fission contribution. The differences in the two approaches therefore arise solely from fission fragments after the r -process freeze-out.

We should point out, however, that the distributions of fission fragments hold at least the same uncertainties as the nuclear reaction rates in the r -process. Our calculations shown in Figure 6 have been performed using the ABLA07 fission fragment distribution model (Kelic et al. 2009). Other fission models predict different distributions (Eichler et al. 2015; Goriely 2015). Nevertheless, the different mechanisms forming the second r -process peak should result in different peak shapes as long as fission produces fragments in the second peak. Following this argumentation, metal-poor stars with larger actinide abundances should also exhibit second peak abundances that reflect the fission fragment production more closely than stars with a lower actinide content.

5. R -process Sites and Their Challenges

This section highlights the agreements and inconsistencies that emerge when we assume that current models of NS–NS mergers or MR SNe are the only source of r -process elements in galaxies. The results of this investigation are summarized in Table 1. In particular, we find that NS–NS mergers alone cannot be consistent with all the observational constraints listed in Section 2. In Section 5.5 we discuss the possibility of multiple sites for the heavy r -process element production.

5.1. Neutron Star Mergers with no DTD

As described in Section 3, delaying the occurrence of NS–NS mergers by a constant coalescence timescale following the lifetime of massive stars (i.e., not taking into account a DTD function) allows GCE simulations to reproduce the decreasing trend of $[\text{Eu}/\text{Fe}]$ in the Galactic disk. If NS–NS mergers are the dominant r -process site, it guarantees a robust r -process pattern for elements between the second and third r -process peaks (see Sections 2.1.1 and Appendix C.1). In addition, they eject a sufficiently large amount of material for each merger event to

explain the large scatter of $[\text{Eu}/\text{Fe}]$ ratios in the metal-poor stars in the Galactic halo (see Section 2.1.3).

However, because this scenario does not use a DTD function for the coalescence times of NS–NS mergers but rather adopts a maximum coalescence time of $\lesssim 100$ Myr, it is incompatible with several observations. In particular, it cannot explain the detection of short GRBs in early-type galaxies (see Section 2.3.1) and the long-lasting DTD functions predicted by population synthesis models (see Section 3.4) and expected theoretically from the wide variety of orbital parameters in binary systems (Rosswog 2015). Furthermore, a constant coalescence time of $\lesssim 100$ Myr is incompatible with the seven known NS–NS binaries with estimated coalescence times ranging from 46 to 2730 Myr (see Tauris et al. 2017 and Section 2.3.2). Finally, this scenario does not allow the gravitational wave event GW170817 to be detected in an early-type galaxy.

5.2. Neutron Star Mergers with a DTD in the Form of t^{-1}

A DTD function in the form of t^{-1} for NS–NS mergers is consistent with the detection of short GRBs (see Section 2.3.2) and the predictions of population synthesis models (see Section 3.4). It is also consistent with the fact that SNe Ia and short GRBs are both detected in similar proportions in early-type galaxies (see Section 2.3), given that most studies agree that SNe Ia do follow a DTD function in the form of t^{-1} as well (but see Heringer et al. 2017). Many GCE simulations have explored the role of NS–NS mergers on the chemical evolution of Eu in the Milky Way using this canonical DTD function. However, as described in Section 3, this scenario does not allow reproducing the decreasing trend of $[\text{Eu}/\text{Fe}]$ in the Galactic disk between $[\text{Fe}/\text{H}] = -1$ and 0, assuming that NS–NS mergers are the only source of heavy r -process elements.

A potential solution to this discrepancy is to claim that short GRB observations suffer from a lack of statistics and that more detections should increase the fraction of short GRBs in late-type star-forming galaxies. This would imply a steeper DTD function for NS–NS mergers (see Section 5.3). Another solution is to assume a flatter DTD function for SNe Ia. This goes in the opposite direction of recent observations, however, which have suggested that if the DTD function of SNe Ia is different than t^{-1} , it should be steeper (Heringer et al. 2017).

5.3. Neutron Star Mergers with Our Exploratory DTDs

As discussed in the last section, using a DTD function in the form of t^{-1} for NS–NS mergers in chemical evolution simulations does not allow reproducing the decreasing trend of $[\text{Eu}/\text{Fe}]$ in the Galactic disk. In this section, we test alternative and exploratory DTD functions, which are shown in the top panel of Figure 7 (see also Simonetti et al. 2019). The idea is to recover the decreasing trend of $[\text{Eu}/\text{Fe}]$ by concentrating the bulk of NS–NS mergers at early times, before the onset of SNe Ia, while still allowing NS–NS mergers to have a wide range of coalescence timescales (up to ~ 10 Gyr). The predictions shown in Figure 7 have been computed with the simple stellar population code SYGMA (Ritter et al. 2018a) and the GCE code OMEGA (Côté et al. 2017b). Both codes are part of the open-source NuPyCEE package.²³

²³ <https://github.com/NuGrid/NuPyCEE>

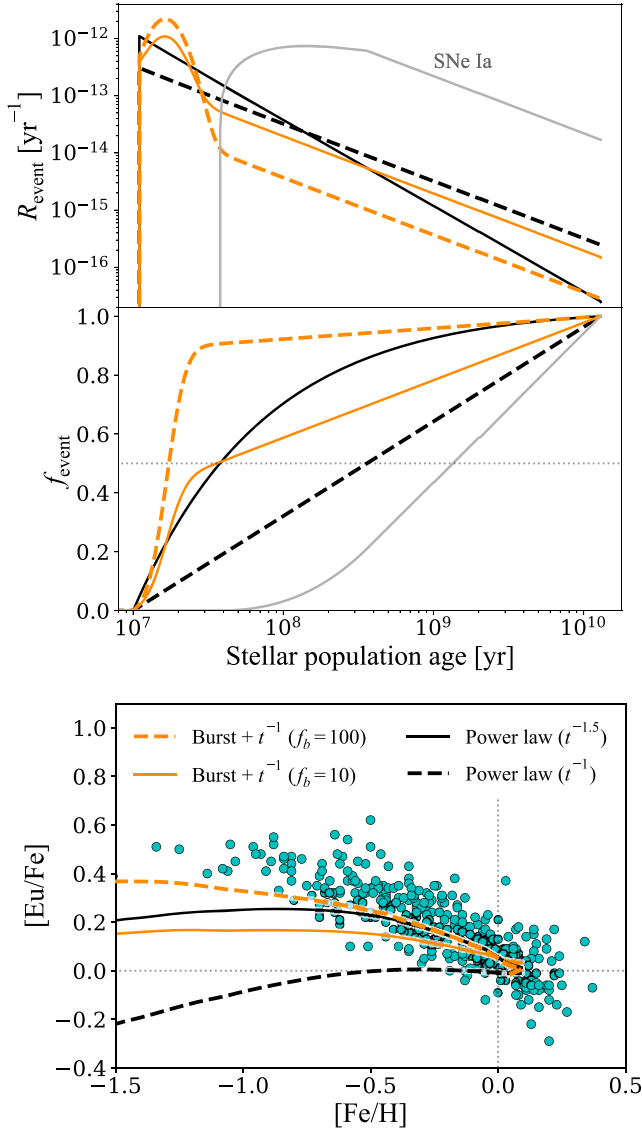


Figure 7. Impact of using different DTD functions for NS–NS mergers on the predicted chemical evolution of Eu. Top panel: four different DTD functions (black and orange lines) in a simple stellar population of $1 M_{\odot}$. When they are integrated, all four DTD functions produce the same number of NS–NS mergers. The gray solid line represents the DTD function used for SNe Ia. Middle panel: cumulated fraction of NS–NS mergers and SNe Ia as a function of time in a stellar population. The dotted horizontal line marks the moment when 50% of the events have occurred. Bottom panel: predicted chemical evolution of $[\text{Eu}/\text{Fe}]$ as a function of $[\text{Fe}/\text{H}]$ using the different DTD functions presented in the top panel. For DTD functions with bursts, f_b is the enhancement factor of the burst relative to the value given by the background power-law distribution. Cyan dots are stellar abundance data for disk stars taken from Battistini & Bensby (2016). The dotted black lines mark the solar values (Asplund et al. 2009).

As shown in the bottom panel of Figure 7, it is possible to recover a decreasing trend for $[\text{Eu}/\text{Fe}]$ using a steep power law in the form of $t^{-1.5}$ (black solid line, see also Côté et al. 2017a and Hotokezaka et al. 2018). This could be in agreement with the $t^{-1.5}$ DTD function derived by D’Avanzo (2015) for short GRBs, although the recent analysis of Fong et al. (2017) rather points toward a function in the form of t^{-1} . We note that some of our population synthesis models do predict DTD functions steeper than t^{-1} (see thick blue line in Figure 4), although the majority are consistent with a t^{-1} distribution. We note that the presence of a third object interacting with an NS–NS binary

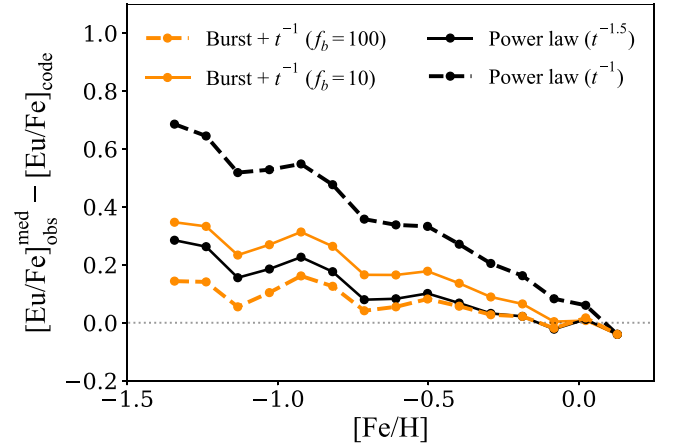


Figure 8. Difference between the $[\text{Eu}/\text{Fe}]$ trends observed in the Galactic disk and predicted using different DTD functions for NS–NS mergers, as presented in Figure 7. For the comparison, we split the $[\text{Fe}/\text{H}]$ axis into bins with constant intervals of 0.105. The dots represent the central value of these bins. For each bin, we calculated the median value of all data present in that bin, and subtracted the predictions made by our code (see Section 5.3). We interpolated our predictions between the time steps in order to recover the values at the central $[\text{Fe}/\text{H}]$ bin points.

could potentially help to concentrate NS–NS mergers at shorter coalescence timescales (Bonetti et al. 2018).

Alternatively, if a strong burst of mergers is assumed before the onset of SNe Ia, followed by a power law in the form of t^{-1} , the decreasing trend of $[\text{Eu}/\text{Fe}]$ can also be recovered (see orange lines in Figure 7). This type of DTD function for NS–NS mergers has been seen in the population synthesis predictions of Dominik et al. (2012), as shown in the lower left panel of their Figure 8. When we use the DTD functions predicted by Dominik et al. (2012), the decreasing trend of $[\text{Eu}/\text{Fe}]$ has been recovered with the GCE code OMEGA (Côté et al. 2017b), as shown with the black solid line in Figure 5 of Mishenina et al. (2017).

Figure 8 shows the difference between the observed chemical evolution trend of $[\text{Eu}/\text{Fe}]$ and the trends predicted using the different DTD functions explored in Figure 7. The steep power law ($t^{-1.5}$) and the DTD with the strongest burst ($f_b = 100$) provide the best fit and generate trends that are consistent within 25% with the median trend observed at $[\text{Fe}/\text{H}] > -0.75$. Overall, the more bulk of Eu is released at an early time, the better the fit (see middle panel of Figure 7).

With the DTD functions explored in this section, more than half of all NS–NS mergers produced by a stellar population will have occurred by ~ 100 Myr (see middle panel of Figure 7). This is because in order to generate a decreasing trend with chemical evolution models, the bulk of Eu must be released before the onset of the Fe production by SNe Ia. However, this significant difference between NS–NS mergers and SNe Ia is currently inconsistent with their similar fraction of occurrence in early-type galaxies (see Section 2.3.1). Furthermore, assuming the DTD functions explored in this section are representative of the real ones, detecting the first gravitational wave signal of an NS–NS merger in an early-type galaxy becomes even more improbable, although not impossible (see Section 2.4.1).

5.4. Rare Classes of Core-collapse Supernovae

Rare classes of CC SNe, such as MR SNe, would naturally explain how Eu can be present in the atmosphere of the most

metal-poor stars (Argast et al. 2004; Matteucci et al. 2014; Cescutti et al. 2015; Wehmeyer et al. 2015; Thielemann et al. 2017; Haynes & Kobayashi 2019). In addition, because the lifetime of massive stars is short relative to the production timescale of Fe in SNe Ia, using CC SNe in GCE simulations allows reproducing the decreasing trend of $[\text{Eu}/\text{Fe}]$ in the Milky Way between $[\text{Fe}/\text{H}] = -1$ and 0 (see Section 3).

Hydrodynamic simulations cannot guarantee that MR SNe will systematically produce the conditions for a robust r -process pattern between the second and third peak, however (see Appendix C.2). While some parts of the ejecta in SNe simulations can synthesize the second and third r -process peaks, there are several other parts (other trajectories) that will mostly produce the first and second peaks alone. When these are summed, it is therefore not guaranteed that the ratio between the second and third r -process peaks will always be similar from one SN to another. If we assume that rare CC SNe are the only source of r -process elements, there is then a potential tension with the robust main r -process abundance pattern observed in r -process enhanced metal-poor stars (see Section 2.1.1). On the other hand, however, these SNe could explain the diversity of abundances for the first-peak elements (see Section 2.1 and Roederer et al. 2010).

This scenario could also be in tension with the high NS–NS merger rate established by LIGO/Virgo (see Section 2.4). When the rate and ejecta of NS–NS mergers are better constrained, we will be in a better situation to quantify how much room there is for additional r -process sites besides NS–NS mergers.

5.5. Multiple r -process Sites Scenario

To summarize the previous sections, neither NS–NS mergers nor MR SNe can reproduce on their own all the observational constraints simultaneously. One solution to this tension is to assume that some of the observational evidence is biased in some way, and that future observations will modify our interpretation of these constraints. If the current observations are representative, however, then there are challenges to be solved. Assuming that future gravitational wave and kilonova detections will prove that NS–NS merger do play an important role in the r -process inventory of the Milky Way, something must be added in chemical evolution simulations in order to recover the decreasing trend of $[\text{Eu}/\text{Fe}]$ in the Galactic disk.

A description of how to reproduce such a decreasing trend was presented in Section 3.1. According to this analysis, the production rate of Eu needs to reach an equilibrium before the onset of SNe Ia. The production rate of Eu from NS–NS mergers does not reach such an equilibrium, however, given the long-lasting nature of their DTD function (see the black dashed line in the top panel of Figure 2). The black solid line in the top panel of that same figure represents the production rate that is required to generate a decreasing trend, as shown in the bottom panel. This rate does not have to come from only one site, however. Indeed, by subtracting the production rate of NS–NS mergers (black dashed line) from the required rate (black solid line), one ends up with a residual production rate, highlighted as the pink dashed line in Figure 2. This residual line represents the production rate that needs to be added to the production rate of NS–NS mergers to recover the decreasing trend of $[\text{Eu}/\text{Fe}]$.

When we assume that NS–NS mergers do contribute to the chemical evolution of Eu in the Milky Way, this suggests that

there should be an additional production site of Eu active in the early universe, at low metallicity (see also A. Skúladóttir et al. 2019, in preparation). To be consistent with chemical evolution studies, this hypothetical additional site should fade away at later times, at higher metallicity. According to Figure 2, NS–NS mergers should become the dominant r -process site roughly when SNe Ia start to bend the $[\text{Eu}/\text{Fe}]$ trend, which roughly corresponds to $[\text{Fe}/\text{H}] \sim -1$ (e.g., Battistini & Bensby 2016; Buder et al. 2018).

By integrating the residual and NS–NS merger lines (dashed lines in Figure 2), about 10% of the current Eu production budget could come from this additional site. With this simple approach, we estimate that this site could have produced 60% and 40% of the Eu during the first 100 Myr and 1 Gyr of Galactic evolution, respectively. These estimates are based on the assumptions that NS–NS mergers have a DTD function of the form t^{-1} , and that the overall production rate needed to fit the evolution of $[\text{Eu}/\text{Fe}]$ is similar to the rate of SNe from massive stars. Furthermore, our estimates depend on the minimum delay time of SNe Ia and are based on the predictions made by a simple toy model that assumes a constant star formation history. To summarize, our estimates are first-order approximations and should serve as a motivation for further studies, rather than be taken for solid predictions.

MR SNe could provide this additional site of Eu production. They require a strong magnetic field to synthesize heavy r -process elements (see also, e.g., Thompson & ud-Doula 2018), and that magnetic field can be amplified by stellar rotation (see Appendix C.2). Because stars are expected to rotate faster at low metallicity (e.g., Maeder et al. 1999; Maeder & Meynet 2001; Martayan et al. 2007), it is possible that MR SNe would preferentially produce the heavy r -process elements in the early universe, while they would mostly produce lighter r -process elements (lighter than Eu) at higher metallicity. In addition, because the nucleosynthesis in MR SNe is not expected to always reach the second and third r -process peak, they could explain the patterns of limited r -process metal-poor stars (see Section 2.1.2 and Hansen et al. 2014; Spite et al. 2018), a pattern that is unlikely to occur when all ejecta components of an NS–NS merger are summed.

BH–NS mergers could also be this additional site, as long as their contribution peaks at low metallicity. However, as shown in Figure 5, the DTD function of BH–NS mergers might not be steep enough to generate a significant boost of Eu before the onset of SNe Ia. More investigation is needed to validate this scenario. BH–NS mergers will hopefully be discovered in the next observing run of LIGO/Virgo. We stress that any other site that for some reason has a peak of Eu production in the early universe is a viable candidate.

We note that previous chemical evolution studies also suggested that SNe alongside with NS–NS mergers should contribute to the chemical evolution of Eu (Argast et al. 2004; Matteucci et al. 2014; Cescutti et al. 2015; Wehmeyer et al. 2015; Haynes & Kobayashi 2019). Although complementary to our work, this was motivated by the difficulty to inject r -process elements early enough to explain the Eu abundances in metal-poor stars (see also Safarzadeh et al. 2018). Here we suggest the possible contribution of an additional site to solve the problem of reproducing the decreasing trend of $[\text{Eu}/\text{Fe}]$ in the Galactic disk, a cleaner feature that is the result of ~ 12 Gyr of chemical evolution in a less stochastic environment. In addition, our scenario strictly requires that the contribution of

this additional r -process site fades away as a function of time and metallicity (pink line in Figure 1). This scenario has also been worked out in parallel by Siegel et al. (2018), who suggested that a metallicity-dependent second r -process site (the collapsars), combined with NS–NS mergers, can help to recover the decreasing trend of [Eu/Fe].

As described in Section 3.4, tighter orbital separations in binary systems can lead to steeper DTD functions for NS–NS mergers. When we assume that the orbital separation distribution of massive stars was steeper at low metallicity, we could theoretically predict a burst of NS–NS mergers in the early universe, while still recovering a DTD function in the form of t^{-1} at current time (at low redshift). This idea is explored in Simonetti et al. (2019) and could provide a potential solution for the inconsistencies highlighted in Table 1, even with NS–NS mergers only. Furthermore, Schönrich & Weinberg (2019) suggested that the decreasing trend problem for [Eu/Fe] could potentially be solved by accounting for a multiphase interstellar medium where NS–NS would preferentially deposit their ejecta in a cold gas component, instead of a hot gas component in which core-collapse supernovae deposit their ejecta. This represents a motivation for future studies to better understand the mixing process of r -process elements in the early universe.

6. Future Studies

In this section, we discuss the current state of the hydrodynamic simulations used to calculate r -process nucleosynthesis in compact binary mergers and CC SNe, and provide guidance for future work to address the tensions highlighted in this paper.

6.1. Simulations of Compact Binary Mergers

Most hydrodynamic simulations of compact binary mergers agree on the amount of dynamical mass ejected and on the impact of the mass asymmetry between the two merging objects (see, e.g., Table 1 in Horowitz et al. 2018). However, there are disagreements regarding the properties of the ejecta.

Neutrino interactions can change the electron fraction of the ejecta and therefore the r -process nucleosynthesis (e.g., Wanajo et al. 2014). Detailed neutrino Boltzmann transport is currently not possible for compact binary merger simulations, and approximations must be made (e.g., Fujibayashi et al. 2017; Kyutoku et al. 2018). Furthermore, the neutrino luminosities and energies depend on the uncertain equation of state (e.g., Sekiguchi et al. 2015; Bovard et al. 2017). Improvements in all these aspects are necessary in order to reliably constrain the range of electron fractions in all ejecta components of compact binary mergers. In addition, magnetohydrodynamical effects can influence the behavior of the dynamical and disk ejecta, but only a few codes currently include them (Palenzuela et al. 2015; Ciolfi et al. 2017; Siegel & Metzger 2018).

A further challenge is the need for high spatial resolution simulations, as all relevant features of the merger need to be resolved (e.g., Kelvin–Helmholtz instabilities at the contact interface). Simulations also need a high temporal resolution because the ejecta leave the computational domain after only a few milliseconds. In the rare cases where the ejecta were followed for a longer time, the ejecta distribution at the end of the initial simulation was mapped to a different code (Rosswog et al. 2014; Roberts et al. 2017; Martin et al. 2018) in order to

study the impact of different heating sources on the dynamical ejecta.

Consistent long-term simulations, which extend to about one second or longer, with an accretion disk and the emergence of a hypermassive neutron star that eventually collapses into a black hole would considerably improve the predictive power of compact binary merger simulations. Further investigations of the impact of nuclear heating on the dynamical ejecta (Rosswog et al. 2014) as well as further increasing the parameter space of NS–NS and NS–BH merger simulations (masses, spins, etc.) are also promising paths to follow in the future.

6.2. Simulations of Core-collapse Supernovae

The initial conditions of MR SN simulations come from previously calculated stellar evolution models, and these include several uncertainties and simplifications. Because of the resulting uncertain magnetic field strengths, the magnetic field is artificial enhanced or decreased in MR SN simulations. In addition, there are small-scale turbulences and instabilities such as the MR instability (e.g., Obergaulinger et al. 2009) that can amplify the magnetic field. To resolve such small-scale effects, however, high-resolution and thus computationally expensive simulations are needed (Mösta et al. 2017; Nishimura et al. 2017). Studies that follow explosions for one or two seconds with 3D simulations including detailed neutrino transports and general relativity will help to understand the dynamic of MR SNe in greater detail.

6.3. Impact of Natal Kicks

We did not include natal kicks in our study that are imparted onto neutron stars after the explosion of their progenitor stars (see Tauris et al. 2017 for a review). Depending on the coalescence timescales of NS–NS mergers and on the velocity of these kicks, it is possible for NS–NS binaries to merge outside galaxies (e.g., Bloom et al. 1999; Fryer et al. 1999; Belczynski et al. 2006; Zemp et al. 2009; Kelley et al. 2010; Behroozi et al. 2014; Safarzadeh & Côté 2017). The simulations of Safarzadeh & Scannapieco (2017) showed that the spatial location of NS–NS mergers can play an important role in the amount of r -process material that is recycled into stars.

If the NS–NS mergers that occur outside galaxies are those that have the longest coalescence times, NS–NS mergers with short coalescence times would then be those that actively participate in the enrichment of Eu inside galaxies. From the point of view of GCE modeling, this would be similar to using a DTD function truncated at some given timescale. If that timescale is similar to or shorter than the delay time needed for SNe Ia to appear in the lifetime of stellar populations, this would be sufficient to reproduce the decreasing trend of [Eu/Fe] in the Galactic disk. In that case, however, the total number of NS–NS mergers would need to be increased in order to account for those that inject Eu outside the star-forming regions. This scenario is to be confirmed or disproved by future studies.

6.4. Actinides

Actinide abundances in metal-poor stars could hold the key to distinguish the hydrodynamical environment(s) of the r -process. The existence of stars with super- and subsolar

actinide yields (Schatz et al. 2002; Roederer et al. 2009; Holmbeck et al. 2018; Ji & Frebel 2018) possibly indicates varying r -process conditions. The fact that all currently known actinide-boost stars are very metal-poor ($[\text{Fe}/\text{H}] \lesssim -2.0$) is another interesting finding. The fraction of actinide-boost stars and the Th/Eu ratios in metal-poor stars could potentially be used as an additional diagnostic tool to probe the contribution of different r -process sites. Astrophysical models of dynamical and disk ejecta in neutron star mergers predict suitable environments for actinide production, and several MR SN models can also provide the required conditions. Progress is needed before we will be able to quantify the typical mass of actinides ejected by NS–NS mergers and MR SNe (see Sections 6.1 and 6.2).

There might also be a possibility to infer actinide yields from direct kilonova observations. Barnes et al. (2016) and Rosswog et al. (2017a) showed that actinides undergoing α -decay could represent an important contribution to the total nuclear heating that powers the kilonova from a few days after the merger onward. Furthermore, Zhu et al. (2018) showed that given its half-life of ~ 60 days, the fission of ^{254}Cf could be detectable several days after an NS–NS merger event, and could potentially be seen in the mid-infrared band of future kilonova light curves.

6.5. Possible Production of Europium by the i -process

The r -process solar residual pattern does not take into account the potential contribution of the i -process (Cowan & Rose 1977). The i -process can be activated at all metallicities in massive stars (even down to metal-free stars, e.g., Banerjee et al. 2018; Clarkson et al. 2018), in rapidly accreting white dwarfs (Denissenkov et al. 2017), and in AGB and post-AGB stars of different types (e.g., Herwig et al. 2011; Jones et al. 2016). Observations of possible i -process abundance signatures have been detected in metal-poor stars (e.g., Dardelet et al. 2014; Lugaro et al. 2015; Abate et al. 2016; Hampel et al. 2016; Roederer et al. 2016a) and in young open stellar clusters (Mishenina et al. 2015) for different elements including Eu all the way up to Pb.

In the simulations of Bertolli et al. (2013) and Dardelet et al. (2014), who considered an i -process activation between ~ 1 hr and ~ 1 day, the $^{151}\text{Eu}/^{153}\text{Eu}$ isotopic ratio varies between 0.7 and 1.5, which is close to the solar value of 0.92. In spite of this interesting result, it does not necessarily mean that the i -process significantly contributed to the total amount of Eu found in the Milky Way. Because of the complex hydrodynamic simulations required to constrain the stellar conditions where the i -process takes place (e.g., Herwig et al. 2014; Woodward et al. 2015), and because of the large uncertainties in nuclear physics (Côté et al. 2018a; Denissenkov et al. 2018), it is currently difficult to quantify the i -process contribution to the solar composition. In addition, large uncertainties in r -process nucleosynthesis calculations (e.g., Mumpower et al. 2016; Thielemann et al. 2017; Horowitz et al. 2018) do not allow us at the moment to derive strong constraints on the i -process component.

The conclusions presented in this paper are drawn under the assumption that the i -process does not contribute to the current inventory of Eu in our Galaxy. More investigations are needed to validate or invalidate this assumption.

7. Conclusions

In this work, we compiled and analyzed a series of observational evidence that probed the properties of r -process sites, and addressed them using nucleosynthesis calculations, population synthesis models, and GCE simulations. At the moment, we cannot build a consistent picture when we assume that there is only one r -process site for elements between the second and third r -process peak. The list of agreements and inconsistencies is shown in Table 1.

It is not possible to reproduce the decreasing trend of $[\text{Eu}/\text{Fe}]$ in the Galactic disk with NS–NS mergers only using a DTD function in the form of t^{-1} for the distribution of their coalescence timescales (see Sections 3.2 and 5.2). This, however, is the form currently predicted by population synthesis models (see Section 3.4) and inferred from short GRB detections (see Section 2.3.2). We can reproduce the decreasing trend by steepening the slope of the DTD function (see also Côté et al. 2017a and Hotokezaka et al. 2018), or by adding a burst of NS–NS mergers before the onset of SNe Ia on top of a t^{-1} distribution (see Section 5.3). This is not consistent with the similar distribution of short GRBs and SNe Ia in early-type galaxies, however (see Section 2.3.1). Assuming a constant short delay time for NS–NS mergers is inconsistent with several observations (see Section 5.1), including the detection of GW170817 in an early-type galaxy.

Because nucleosynthesis calculations show that NS–NS mergers are able to produce a robust r -process pattern (see Appendix C.1), and because the merger rate established by LIGO/Virgo is significantly high (see Section 2.4.3), NS–NS mergers are likely to play an important role in the evolution of r -process elements. If that is the case, and if we assume that the current observational constraints are all reliable, then one solution is to involve a second r -process site in the early universe that is capable of producing Eu (see Section 5.5). This additional site should fade away at later times, at higher metallicity (see the pink dashed line in Figure 2), and would roughly account for $\sim 50\%$ of the Eu produced in the early universe, and $\sim 10\%$ of all Eu currently present in the Milky Way. This is a plausible solution, but it does not mean that it is the correct solution.

MR SNe could be this additional site of Eu. To reach the third r -process peak and produce Eu along the way, these SNe need very strong magnetic fields (see Appendix C.2). Because massive stars are likely to rotate faster at low metallicity, the magnetic field present during an MR SN could also be higher at low metallicity, which would explain why this second site fades away at higher metallicity (see Section 5.5). This conclusion is based on the chemical evolution of the Galactic disk, which encodes most of the evolution history of the Milky Way. We note that any other production site of Eu that respects this metallicity dependency is a possible candidate.

Although we presented a possible solution to the current interdisciplinary tensions, the information shown in Table 1 should be taken as the starting point for future work. Other possible solutions exist (e.g., Sections 6.3 and 6.5), and further observations might change our interpretation of the observational evidence listed in Section 2. In particular, more detections of NS–NS mergers by LIGO/Virgo and improvements in the interpretation of kilonova light curves will better define how much room there is for other r -process sites.

We are thankful to Erika Holmbeck and Ian Roederer for discussions on the abundances of metal-poor stars, to Gabriele Cescutti for discussions on modeling neutron-capture elements in a chemical evolution framework, and to Mohammadtaher Safarzadeh for discussions on the impact of natal kicks. This research is supported by the ERC Consolidator Grant (Hungary) funding scheme (project RADIOSTAR, G.A. n. 724560) and by the National Science Foundation (USA) under grant No. PHY-1430152 (JINA Center for the Evolution of the Elements). This paper included work from the ChETEC (Chemical Elements as Tracers of the Evolution of the Cosmos) COST Action (CA16117), supported by COST (European Cooperation in Science and Technology), and has benefited from discussions at the 2018 Frontiers in Nuclear Astrophysics Conference supported by the JINA Center for the Evolution of the Elements. A.A., M.E., and M.R. were supported by the ERC starting grant EUROPIUM (grant No. 677912) and BMBF under grant No. 05P15RDFN1. M.E. is also supported by the Swiss National Foundation (Project No. P2BSP2_172068). A.F. is partially supported by NSF-CAREER grant AST-1255160 and NSF grant 1716251. M.P. acknowledges the support of STFC through the University of Hull Consolidated Grant ST/R000840/1 and ongoing resource allocations on the University of Hulls High Performance Computing Facility viper. K.B. acknowledges support from the Polish National Science Center (NCN) grant: Sonata Bis 2 DEC-2012/07/E/ST9/01360. F.M. was supported by funds from Trieste University (FRA2016).

Software: JINABase (Abomalima & Frebel 2017), OMEGA (Côté et al. 2017b), SYGMA (Ritter et al. 2018a), StarTrack (Belczynski et al. 2002, 2008), matplotlib (<https://matplotlib.org>), NumPy (Van Der Walt et al. 2011).

Appendix A

Minimum Delay Time and Star Formation History

In Section 3.2 we mentioned that GCE predictions for $[\text{Eu}/\text{Fe}]$ at $[\text{Fe}/\text{H}] > -1$ are insensitive to the minimum delay time of NS–NS mergers when we adopt the constant delay-time approximation. In this section, we test this statement when we adopt a DTD function of the form t^{-1} , using $t_{\text{min}} = 1, 10,$ and 100 Myr, where t_{min} refers to the minimum delay time between the formation of the progenitor stars and the merger event. We note that according to the population synthesis predictions presented in Figure 4, t_{min} is typically below 100 Myr. As shown in Figure 9, using the GCE code OMEGA, the predicted trends at $[\text{Fe}/\text{H}] > -1$ are similar when a constant delay time is used (blue band, see also Matteucci et al. 2014; Cescutti et al. 2015; Côté et al. 2017a), but are significantly different when a DTD function is used (black band). Nevertheless, varying t_{min} can still not provide a good agreement with the measured $[\text{Eu}/\text{Fe}]$ trend when a DTD function is used in the form of t^{-1} . This parameter therefore does not affect the general conclusions of this work, although it could affect the estimated contribution of the hypothetical additional r -process site (see Section 5.5).

As a complement, we also explored the impact of the star formation history (see also Hotokezaka et al. 2018). Figure 10 shows the predictions made by the OMEGA code when a decreasing star formation history (solid lines) and a constant star formation history are used (dashed lines). Overall, we find that the effect of the star formation history is minor in comparison to the effect of using different delay time assumptions for NS–NS mergers. As in Figure 7 of Hotokezaka

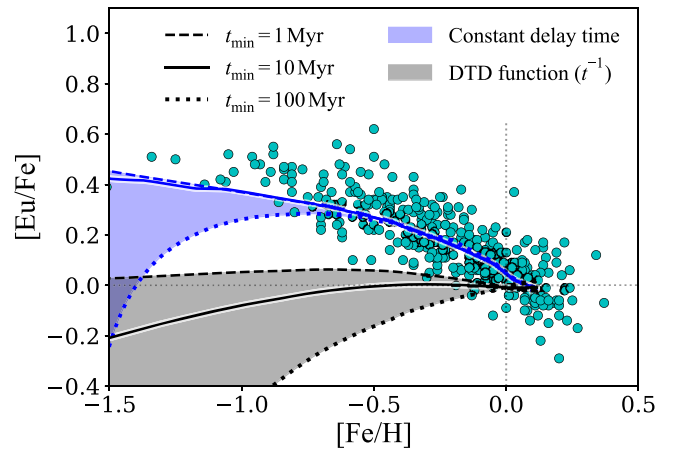


Figure 9. Impact of using different minimum delay times for NS–NS mergers on the predicted chemical evolution of Eu. The blue and black bands show the prediction when constant delay times or delay-time distribution (DTD) functions are assumed, respectively. The dashed, solid, and dotted lines show the predictions for different minimum delay times between the formation of the progenitor stars and the onset of NS–NS mergers. In the case of constant delay times, the minimum delay times are the constant delay times. Cyan dots are stellar abundance data for disk stars taken from Battistini & Bensby (2016). The dotted black lines mark the solar values (Asplund et al. 2009).

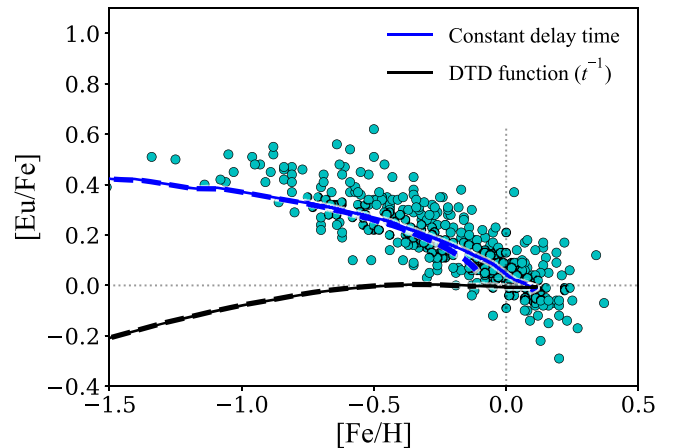


Figure 10. Impact of using different star formation histories on the predicted chemical evolution of Eu with NS–NS mergers. The blue lines show predictions when we assume that NS–NS mergers all occur after a constant delay time of 10 Myr following the formation of progenitor stars, while the black lines show predictions when we assume a DTD function of the form t^{-1} . The solid lines show results with a decreasing star formation history, from $11 M_{\odot} \text{ yr}^{-1}$ at time zero down to $2 M_{\odot} \text{ yr}^{-1}$ after 13 Gyr, while the dashed lines show results with a constant star formation history of $6 M_{\odot} \text{ yr}^{-1}$. All simulations generate a current stellar mass of $5 \times 10^{10} M_{\odot}$. Cyan dots are stellar abundance data for disk stars taken from Battistini & Bensby (2016). The dotted black lines mark the solar values (Asplund et al. 2009).

et al. (2018), the maximum $[\text{Fe}/\text{H}]$ reached by our predictions is shifted to lower $[\text{Fe}/\text{H}]$ values when a constant star formation history is used (dashed lines), likely because of the larger amount of infalling gas compared to the decreasing star formation history, which has a current star formation rate three times lower than in the constant case. Overall, as for the minimum delay time for NS–NS mergers, the adopted star formation history should not affect the general conclusions of this work.

Appendix B

Population Synthesis: Brief Description of Adopted Models

Here we discuss the properties of the population synthesis models adopted for our study in more detail (see Section 3.4). We use the upgraded population synthesis code *StarTrack* (Belczynski et al. 2002, 2008). Improvements relevant for massive stars include a better treatment of the common envelope evolution (Dominik et al. 2012) and a remnant mass prescription (Fryer et al. 2012) that reproduces the first gap found in between the observed mass distributions of neutron stars and black holes in the Milky Way (Belczynski et al. 2012). Effects of pair-instability pulsation SNe and pair-instability SNe are taken into account because they are believed to create the second mass gap in the observed mass distribution of compact objects (Belczynski et al. 2016).

We account for the formation of neutron stars through electron-capture SNe (e.g., Miyaji et al. 1980; Podsiadlowski et al. 2004; Chruslinska et al. 2018) and through accretion-induced collapse of white dwarfs (e.g., Nomoto & Kondo 1991; Ruitter et al. 2018). The maximum mass of neutron stars is set to $2.5 M_{\odot}$, which is consistent with the highest-mass known neutron stars of $2.3 M_{\odot}$ (Linares et al. 2018). The initial conditions of the binary systems are constrained by observations (de Mink & Belczynski 2015). The differences between the models can also be seen in Figures 4 and 5 in the main body of this article. Model M10 represents the standard input physics in *StarTrack*. In particular, the natal kick velocities initially imparted on black holes are small, and in some cases non-existent. For neutron stars, the natal kicks are defined by a Maxwellian distribution with $\sigma = 265 \text{ km s}^{-1}$. However, the exact values of the natal kicks can be altered by the amount of material falling back onto the compact objects after the SN explosions (see Belczynski et al. 2017b for details). The magnitude of natal kicks is an important quantity because it can significantly modify the coalescence timescales of NS–NS and BH–NS systems (e.g., Belczyński & Bulik 1999).

The M13 model is similar to the M10 model, but the Maxwellian natal kick distribution with $\sigma = 265 \text{ km s}^{-1}$ is adopted for both black holes and neutron stars. In addition, the amount of fallback does not regulate the kick velocities. We note that neutron stars formed by electron-capture SNe and by the accretion-induced collapse of white dwarfs still have natal kicks set to zero, as is the case for all models presented in this section.

In model M20, the natal kick prescription for black holes and neutron stars is the same as in the M10 model, but the input physics describing the evolution of binary systems during the common envelope phase is modified. This includes, for example, 80% non-conservative Roche Lobe overflow and 5% Bondi-Hoyle rate accretion, as opposed to 50% and 10%, respectively, in the M10 model (see Belczynski et al. 2017b for details).

The M23, M25, and M26 models have the same modified input physics as in the M20 model, but adopt a Maxwellian natal kick velocity distribution for both neutron stars and black holes, as in Model M13. The dispersion velocity σ for models M23, M25, and M26 is 265, 130, and 70 km s^{-1} , respectively.

Appendix C

R-process Nucleosynthesis in Different Environments

C.1. Neutron Star Mergers

In NS–NS mergers, there are various ways of ejecting matter, and they lead to different conditions and nucleosynthesis. The total amount of ejecta depends on the configuration of the binary system (e.g., neutron star masses and eccentricity of the orbit). For the dynamical ejecta, between about 10^{-3} and $10^{-2} M_{\odot}$ of very neutron-rich (low Y_e) material can be ejected by means of tidal effects or shocks in the interaction zone between the two neutron stars. These numbers are in agreement with estimates of the ejected mass for GW170817 (see Section 2.4.2), and are large enough to recover the scatter seen in the [Eu/Fe] abundances of metal-poor stars (see Section 2.1.3).

The dynamical ejecta robustly produce the heavy r -process nuclei from the second peak up to the actinide region with mass numbers A above 200. The extreme neutron-richness of the dynamical ejecta leads to fission cycling and an r -process path close to the neutron drip line (further favored by rapid expansion/cooling). As a consequence, this environment only produces nuclei from the typical fission fragment mass numbers $A \approx 120$ and larger. They do not produce the lighter first-peak r -process nuclei. NS–NS mergers are thus consistent with the robust main r -process patterns seen in metal-poor stars (Snedden et al. 2008, see also Section 2.1).

However, other hydrodynamical codes lead to broader ranges in electron fraction and entropy (Bauswein et al. 2013; Sekiguchi et al. 2015; Foucart et al. 2016; Radice et al. 2016; Bovard et al. 2017). Simulations that incorporate general relativity effects exhibit a more energetic collision because the neutron star radii are smaller. This leads to strong shocks that increase the Y_e and the entropy in the ejecta. Even these simulations produce robust abundances between the second and third r -process peak, however, because the ejecta consist of two main components: those that stop at or before the second peak, and those that produce the full mass range of r -process nuclei up to the actinides in a robust way. Some recent works have found conditions with low Y_e and high entropies (related to shocked ejecta with very fast expansion velocities), which result in an unusual abundance pattern (reported, e.g., in Metzger et al. 2015; Barnes et al. 2016; Bovard et al. 2017). However, these conditions contribute to only a very small fraction of the total ejecta, and therefore have no real effect on the integrated abundances.

In addition to the dynamical ejecta, other mass-loss channels operate on longer timescales that are related to the formation of a post-merger disk around the central remnant object (Beloborodov 2008; Dessart et al. 2009; Foucart 2012; Fernández & Metzger 2013; Perego et al. 2014; Fernández et al. 2015; Just et al. 2015; Martin et al. 2015; Siegel & Metzger 2017). Again, the formation of the disk and its mass depend on the binary system configuration. If the central object does not promptly collapse into a black hole, it emits neutrinos, which together with the neutrinos emitted from the disk can generate a mass outflow similar to neutrino-driven winds in CC SNe (Perego et al. 2014; Just et al. 2015; Martin et al. 2015). Simulations also show that disk material can become gravitationally unbound by means of viscous effects and nuclear recombination (Fernández & Metzger 2013; Fernández et al. 2015; Just et al. 2015). Because the timescales of these

ejecta are longer, they are exposed to neutrinos for a longer time than the dynamical ejecta. Because neutrinos transform neutrons into protons, these longer-timescale ejecta are typically less neutron-rich.

While the viscous ejecta can still produce the r -process nuclei with the highest masses (Wu et al. 2016), the neutrino-driven ejecta have been found to only produce first-peak elements (Perego et al. 2014; Martin et al. 2015). The viscous and the neutrino-driven ejecta represent about 5%–20% (Fernández & Metzger 2013; Fernández et al. 2015; Just et al. 2015) and 5% (Martin et al. 2015) of the initial disk mass, respectively. These numbers depend on the fate of the central remnant. For example, a quicker collapse into a black hole leads to a lower ejected mass through these two mass-loss channels. Finally, magnetic fields can also contribute to the acceleration and ejection of mass (Siegel & Metzger 2017). However, only preliminary results are available, and it is still too early to make conclusive statements about the importance of magnetic fields.

C.2. Core-collapse Supernovae

At the surface of a proto-neutron star, electron capture can deleptonize the material. If this material is ejected, it can produce r -process elements. In standard CC SNe, however, the matter is mainly ejected by neutrinos, which reduce the number of neutrons by converting them into protons. In such conditions, current simulations indicate that standard CC SNe could at most produce trans-iron elements such as Sr, Y, Zr, Mo, and Ru (first-peak elements), and perhaps in some cases elements up to Ag (e.g., Roberts et al. 2010; Arcones & Montes 2011; Bliss et al. 2018; Eichler et al. 2018 and references therein). In order to produce heavier elements such as Eu, another ejection mechanism is necessary. Magnetic fields and rotation have been identified as a possibility by Cameron (2003) and Nishimura et al. (2006). Simulations of MR SNe have become possible at least with simplifications in the neutrino transport. We refer to the introduction of Section 4 for a list of other possible r -process sites.

Based on 3D simulations with a simple leakage treatment for the neutrinos, Winteler et al. (2012) found that the heavy r -process can be synthesized in MR SNe. The 2D simulations of Nishimura et al. (2015, 2017) with parametric neutrino treatment found that when the magnetic field is strong and neutrino emission is reduced, a jet-like explosion develops and neutron-rich material is ejected. Again with a strong magnetic field, Mösta et al. (2017) have shown, however, that in 3D simulations it becomes harder to reach the neutron-richness required for a robust r -process. They also confirm the results of Nishimura et al. (2015), demonstrating that when the neutrino emission is artificially increased, it reaches from producing a robust r -process to producing a weak r -process up to only the second peak.

This behavior could potentially explain the abundance patterns of metal-poor stars, such as HD 122563 (Honda et al. 2006), enhanced in Sr and other elements at the neutron shell closure $N = 50$ relative to Ba. Furthermore, because MR SNe might synthesize a variety of r -process abundance patterns depending on the conditions, from a weak to a robust r -process including the second and third peaks, such SNe could explain the variety of metal-poor stars having abundance patterns in between stars like HD 122563 and stars showing the full r -process pattern (see Roederer et al. 2010). Improved

neutrino transport is mandatory before we can reach any definite conclusions because neutrinos can lead to a broad variability in the conditions of the ejected matter (Obergaullinger & Aloy 2017; M. Reichert et al. 2019, in preparation).

Regarding the total amount of r -process ejected material, MR SNe may contribute very differently depending on the strength of the magnetic field. In general, the ejected mass containing r -process elements will be higher than with neutrino-driven winds in regular CC SNe, but will be lower than with NS–NS mergers. This type of explosions is expected to occur in a few percent of all SNe at most, preferentially at low metallicities where the magnetic field could be amplified by faster stellar rotation velocities. Because of this possible dependence on metallicity, MR SNe represent an interesting candidate for our multiple r -process sites scenario that we presented in Section 5.5.

ORCID iDs

Benoit Côté  <https://orcid.org/0000-0002-9986-8816>
 Marius Eichler  <https://orcid.org/0000-0002-4445-8908>
 Camilla J. Hansen  <https://orcid.org/0000-0002-7277-7922>
 Paolo Simonetti  <https://orcid.org/0000-0002-7744-5804>
 Anna Frebel  <https://orcid.org/0000-0002-2139-7145>
 Chris L. Fryer  <https://orcid.org/0000-0003-2624-0056>
 Marco Pignatari  <https://orcid.org/0000-0002-9048-6010>
 Moritz Reichert  <https://orcid.org/0000-0001-6653-7538>
 Francesca Matteucci  <https://orcid.org/0000-0001-7067-2302>

References

- Abate, C., Stancliffe, R. J., & Liu, Z.-W. 2016, *A&A*, 587, A50
 Abbott, B. P., Abbott, R., Abbott, T. D., et al. 2017a, arXiv:1710.05836
 Abbott, B. P., Abbott, R., Abbott, T. D., et al. 2017b, *ApJL*, 848, L13
 Abbott, B. P., Abbott, R., Abbott, T. D., et al. 2017c, *PhRvL*, 119, 161101
 Abbott, B. P., Abbott, R., Abbott, T. D., et al. 2017d, *ApJL*, 848, L12
 Abohalima, A., & Frebel, A. 2017, arXiv:1711.04410
 Aoki, W., Beers, T. C., Lee, Y. S., et al. 2013, *AJ*, 145, 13
 Arcavi, I., Hosseinzadeh, G., Howell, D. A., et al. 2017, *Natur*, 551, 64
 Arcones, A., & Montes, F. 2011, *ApJ*, 731, 5
 Arcones, A., & Thielemann, F.-K. 2013, *JPhG*, 40, 013201
 Argast, D., Samland, M., Thielemann, F.-K., & Qian, Y.-Z. 2004, *A&A*, 416, 997
 Arlandini, C., Käppeler, F., Wisshak, K., et al. 1999, *ApJ*, 525, 886
 Arnould, M., Goriely, S., & Takahashi, K. 2007, *PhR*, 450, 97
 Asplund, M., Grevesse, N., Sauval, A. J., & Scott, P. 2009, *ARA&A*, 47, 481
 Banerjee, P., Qian, Y.-Z., & Heger, A. 2018, *ApJ*, 865, 120
 Barklem, P. S., Christlieb, N., Beers, T. C., et al. 2005, *A&A*, 439, 129
 Barnes, J., & Kasen, D. 2013, *ApJ*, 775, 18
 Barnes, J., Kasen, D., Wu, M.-R., & Martínez-Pinedo, G. 2016, *ApJ*, 829, 110
 Battistini, C., & Bensby, T. 2016, *A&A*, 586, A49
 Bauswein, A., Goriely, S., & Janka, H.-T. 2013, *ApJ*, 773, 78
 Beers, T. C., & Christlieb, N. 2005, *ARA&A*, 43, 531
 Behroozi, P. S., Ramirez-Ruiz, E., & Fryer, C. L. 2014, *ApJ*, 792, 123
 Belczynski, K., Askar, A., Arca-Sedda, M., et al. 2017a, *A&A*, 615, 91
 Belczynski, K., Askar, A., Arca-Sedda, M., et al. 2018a, *A&A*, 615, A91
 Belczyński, K., & Bulik, T. 1999, *A&A*, 346, 91
 Belczynski, K., Bulik, T., Olejak, A., et al. 2018b, arXiv:1812.10065
 Belczynski, K., Heger, A., Gladysz, W., et al. 2016, *A&A*, 594, A97
 Belczynski, K., Kalogera, V., & Bulik, T. 2002, *ApJ*, 572, 407
 Belczynski, K., Kalogera, V., Rasio, F. A., et al. 2008, *ApJS*, 174, 223
 Belczynski, K., Klencki, J., Meynet, G., et al. 2017b, arXiv:1706.07053
 Belczynski, K., Perna, R., Bulik, T., et al. 2006, *ApJ*, 648, 1110
 Belczynski, K., Wiktorowicz, G., Fryer, C. L., Holz, D. E., & Kalogera, V. 2012, *ApJ*, 757, 91
 Beloborodov, A. M. 2008, in AIP Conf. Proc. 1054, Cool Disks, Hot Flows: The Varying Faces of Accreting Compact Objects, ed. M. Axelsson (New York: AIP), 51
 Bensby, T., Feltzing, S., & Oey, M. S. 2014, *A&A*, 562, A71

- Berger, E. 2014, *ARA&A*, 52, 43
- Bertolli, M. G., Herwig, F., Pignatari, M., & Kawano, T. 2013, arXiv:1310.4578
- Beun, J., McLaughlin, G. C., Surman, R., & Hix, W. R. 2006, *PhRvD*, 73, 093007
- Bisterzo, S., Travaglio, C., Gallino, R., Wiescher, M., & Käppeler, F. 2014, *ApJ*, 787, 10
- Blanchard, P. K., Berger, E., Fong, W., et al. 2017, *ApJL*, 848, L22
- Bliss, J., Arcones, A., & Qian, Y.-Z. 2018, *ApJ*, 866, 105
- Bloom, J. S., Sigurdsson, S., & Pols, O. R. 1999, *MNRAS*, 305, 763
- Bonetti, M., Perego, A., Capelo, P. R., Dotti, M., & Miller, M. C. 2018, *PASA*, 35, e017
- Bovard, L., Martin, D., Guercilena, F., et al. 2017, *PhRvD*, 96, 124005
- Buder, S., Asplund, M., Duong, L., et al. 2018, *MNRAS*, 478, 4513
- Burris, D. L., Pilachowski, C. A., Armandroff, T. E., et al. 2000, *ApJ*, 544, 302
- Cameron, A. G. W. 2003, *ApJ*, 587, 327
- Cescutti, G., Romano, D., Matteucci, F., Chiappini, C., & Hirschi, R. 2015, *A&A*, 577, A139
- Chiappini, C., Matteucci, F., & Gratton, R. 1997, *ApJ*, 477, 765
- Chornock, R., Berger, E., Kasen, D., et al. 2017, *ApJL*, 848, L19
- Christlieb, N., Gustafsson, B., Korn, A. J., et al. 2004, *ApJ*, 603, 708
- Chruslinska, M., Belczynski, K., Klencki, J., & Benacquista, M. 2018, *MNRAS*, 474, 2937
- Ciolfi, R., Kastaun, W., Giacomazzo, B., et al. 2017, *PhRvD*, 95, 063016
- Clarkson, O., Herwig, F., & Pignatari, M. 2018, *MNRAS*, 474, L37
- Connelly, J. N., Bollard, J., & Bizzarro, M. 2017, *GeCoA*, 201, 345
- Côté, B., Belczynski, K., Fryer, C. L., et al. 2017a, *ApJ*, 836, 230
- Côté, B., Denissenkov, P., Herwig, F., et al. 2018a, *ApJ*, 854, 105
- Côté, B., Fryer, C. L., Belczynski, K., et al. 2018b, *ApJ*, 855, 99
- Côté, B., O'Shea, B. W., Ritter, C., Herwig, F., & Venn, K. A. 2017b, *ApJ*, 835, 128
- Côté, B., Ritter, C., O'Shea, B. W., et al. 2016, *ApJ*, 824, 82
- Coulter, D. A., Foley, R. J., Kilpatrick, C. D., et al. 2017, *Sci*, 358, 1556
- Cowan, J. J., Roederer, I. U., Sneden, C., & Lawler, J. E. 2011, in *RR Lyrae Stars, Metal-Poor Stars, and the Galaxy*, ed. A. McWilliam, Vol. 5 (Pasadena, CA: The Observatories of the Carnegie Institution of Washington), 223
- Cowan, J. J., & Rose, W. K. 1977, *ApJ*, 212, 149
- Cowan, J. J., Sneden, C., Lawler, J. E., et al. 2019, arXiv:1901.01410
- Cowperthwaite, P. S., Berger, E., Villar, V. A., et al. 2017, *ApJL*, 848, L17
- Cristallo, S., Abia, C., Straniero, O., & Piersanti, L. 2015, *ApJ*, 801, 53
- Dardelet, L., Ritter, C., Prado, P., et al. 2014, in *XIII Nuclei in the Cosmos (NIC XIII)*, ed. Z. Elekes & Z. Fülöp (Trieste: SISSA), 145
- D'Avanzo, P. 2015, *JHEAp*, 7, 73
- de Mink, S. E., & Belczynski, K. 2015, *ApJ*, 814, 58
- Denissenkov, P., Perdikakis, G., Herwig, F., et al. 2018, *JPhG*, 45, 055203
- Denissenkov, P. A., Herwig, F., Battino, U., et al. 2017, *ApJL*, 834, L10
- Dessart, L., Ott, C. D., Burrows, A., Rosswog, S., & Livne, E. 2009, *ApJ*, 690, 1681
- Doherty, C. L., Gil-Pons, P., Lau, H. H. B., Lattanzio, J. C., & Siess, L. 2014a, *MNRAS*, 437, 195
- Doherty, C. L., Gil-Pons, P., Lau, H. H. B., et al. 2014b, *MNRAS*, 441, 582
- Domink, M., Belczynski, K., Fryer, C., et al. 2012, *ApJ*, 759, 52
- Drout, M. R., Piro, A. L., Shappee, B. J., et al. 2017, *Sci*, 358, 1570
- Duggan, G. E., Kirby, E. N., Andrievsky, S. M., & Korotin, S. A. 2018, *ApJ*, 869, 50
- Eichler, M., Arcones, A., Kelic, A., et al. 2015, *ApJ*, 808, 30
- Eichler, M., Nakamura, K., Takiwaki, T., et al. 2018, *JPhG*, 45, 014001
- Ezzeddine, R., Frebel, A., & Plez, B. 2017, *ApJ*, 847, 142
- Farouqi, K., Kratz, K.-L., Mashonkina, L. I., et al. 2009, *ApJL*, 694, L49
- Fernández, R., Kasen, D., Metzger, B. D., & Quataert, E. 2015, *MNRAS*, 446, 750
- Fernández, R., & Metzger, B. D. 2013, *MNRAS*, 435, 502
- Fernández, R., & Metzger, B. D. 2016, *ARNPS*, 66, 23
- Few, C. G., Courty, S., Gibson, B. K., Michel-Dansac, L., & Calura, F. 2014, *MNRAS*, 444, 3845
- Fong, W., Berger, E., Blanchard, P. K., et al. 2017, *ApJL*, 848, L23
- Fong, W., Berger, E., Chornock, R., et al. 2013, *ApJ*, 769, 56
- Foucart, F. 2012, *PhRvD*, 86, 124007
- Foucart, F., O'Connor, E., Roberts, L., et al. 2016, *PhRvD*, 94, 123016
- Frebel, A. 2018, *ARNPS*, 68, 237
- Frebel, A., Christlieb, N., Norris, J. E., et al. 2007, *ApJL*, 660, L117
- Frebel, A., & Norris, J. E. 2015, *ARA&A*, 53, 631
- Frischknecht, U., Hirschi, R., Pignatari, M., et al. 2016, *MNRAS*, 456, 1803
- Fröhlich, C., Martínez-Pinedo, G., Liebendörfer, M., et al. 2006, *PhRvL*, 96, 142502
- Fryer, C. L., Belczynski, K., Wiktorowicz, G., et al. 2012, *ApJ*, 749, 91
- Fryer, C. L., Herwig, F., Hungerford, A., & Timmes, F. X. 2006, *ApJL*, 646, L131
- Fryer, C. L., Woosley, S. E., & Hartmann, D. H. 1999, *ApJ*, 526, 152
- Fujibayashi, S., Sekiguchi, Y., Kiuchi, K., & Shibata, M. 2017, *ApJ*, 846, 114
- Gallino, R., Arlandini, C., Busso, M., et al. 1998, *ApJ*, 497, 388
- Giacobbo, N., & Mapelli, M. 2018, *MNRAS*, 482, 2234
- Giacomazzo, B., Perna, R., Rezzolla, L., Troja, E., & Lazzati, D. 2013, *ApJL*, 762, L18
- Gibson, B. K., Fenner, Y., Renda, A., Kawata, D., & Lee, H.-c. 2003, *PASA*, 20, 401
- Gompertz, B. P., Levan, A. J., Tanvir, N. R., et al. 2017, *ApJ*, 860, 62
- González Delgado, R. M., Cid Fernandes, R., Pérez, E., et al. 2016, *A&A*, 590, A44
- Goriely, S. 2015, *EPJA*, 51, 22
- Goriely, S., Bauswein, A., & Janka, H.-T. 2011, *ApJL*, 738, L32
- Graur, O., Bianco, F. B., Huang, S., et al. 2017a, *ApJ*, 837, 120
- Graur, O., Bianco, F. B., Modjaz, M., et al. 2017b, *ApJ*, 837, 121
- Graur, O., Poznanski, D., Maoz, D., et al. 2011, *MNRAS*, 417, 916
- Graur, O., Rodney, S. A., Maoz, D., et al. 2014, *ApJ*, 783, 28
- Greggio, L. 2005, *A&A*, 441, 1055
- Grichener, A., & Soker, N. 2018, arXiv:1810.03889
- Guiglión, G., de Laverny, P., Recio-Blanco, A., & Prantzos, N. 2018, *A&A*, 619, A143
- Hampel, M., Stancliffe, R. J., Lugaro, M., & Meyer, B. S. 2016, *ApJ*, 831, 171
- Hansen, C. J., El-Souri, M., Monaco, L., et al. 2018a, *ApJ*, 855, 83
- Hansen, C. J., Ludwig, H.-G., Seifert, W., et al. 2015a, *AN*, 336, 665
- Hansen, C. J., Montes, F., & Arcones, A. 2014, *ApJ*, 797, 123
- Hansen, T., Hansen, C. J., Christlieb, N., et al. 2015b, *ApJ*, 807, 173
- Hansen, T. T., Holmbeck, E. M., Beers, T. C., et al. 2018b, *ApJ*, 858, 92
- Haynes, C. J., & Kobayashi, C. 2019, *MNRAS*, 483, 5123
- Heringer, E., Pritchett, C., Kezzer, J., et al. 2017, *ApJ*, 834, 15
- Herwig, F., Pignatari, M., Woodward, P. R., et al. 2011, *ApJ*, 727, 89
- Herwig, F., Woodward, P. R., Lin, P.-H., Knox, M., & Fryer, C. 2014, *ApJL*, 792, L3
- Hill, V., Plez, B., Cayrel, R., et al. 2002, *A&A*, 387, 560
- Hirai, Y., Ishimaru, Y., Saitoh, T. R., et al. 2015, *ApJ*, 814, 41
- Holmbeck, E. M., Beers, T. C., Roederer, I. U., et al. 2018, *ApJL*, 859, L24
- Honda, S., Aoki, W., Ishimaru, Y., Wanajo, S., & Ryan, S. G. 2006, *ApJ*, 643, 1180
- Horowitz, C. J., Arcones, A., Côté, B., et al. 2018, arXiv:1805.04637
- Hotokezaka, K., Beniamini, P., & Piran, T. 2018, *IJMPD*, 27, 1842005
- Hotokezaka, K., Piran, T., & Paul, M. 2015, *NatPh*, 11, 1042
- Im, M., Yoon, Y., Lee, S.-K. J., et al. 2017, *ApJL*, 849, L16
- Ishimaru, Y., Wanajo, S., & Prantzos, N. 2015, *ApJL*, 804, L35
- Iwamoto, K., Brachwitz, F., Nomoto, K., et al. 1999, *ApJS*, 125, 439
- Ji, A. P., & Frebel, A. 2018, *ApJ*, 856, 138
- Ji, A. P., Frebel, A., Chiti, A., & Simon, J. D. 2016a, *Natur*, 531, 610
- Ji, A. P., Frebel, A., Simon, J. D., & Chiti, A. 2016b, *ApJ*, 830, 93
- Jones, S., Ritter, C., Herwig, F., et al. 2016, *MNRAS*, 455, 3848
- José, J., & Hernanz, M. 1998, *ApJ*, 494, 680
- Just, O., Bauswein, A., Pulpillo, R. A., Goriely, S., & Janka, H.-T. 2015, *MNRAS*, 448, 541
- Käppeler, F., Beer, H., & Wisshak, K. 1989, *RPPH*, 52, 945
- Karakas, A. I. 2010, in *Principles and Perspectives in Cosmochemistry*, ed. A. Goswami & B. Eswar Reddy (Berlin: Springer), 107
- Kasen, D., Metzger, B., Barnes, J., Quataert, E., & Ramirez-Ruiz, E. 2017, *Natur*, 551, 80
- Kelic, A., Valentina Ricciardi, M., & Schmidt, K.-H. 2009, arXiv:0906.4193
- Kelley, L. Z., Ramirez-Ruiz, E., Zemp, M., Diemand, J., & Mandel, I. 2010, *ApJL*, 725, L91
- Kelvin, L. S., Driver, S. P., Robotham, A. S. G., et al. 2014, *MNRAS*, 444, 1647
- Kennicutt, R. C., Jr. 1998, *ApJ*, 498, 541
- Komiya, Y., & Shigeyama, T. 2016, *ApJ*, 830, 76
- Korobkin, O., Rosswog, S., Arcones, A., & Winteler, C. 2012, *MNRAS*, 426, 1940
- Kriszianas, K., Contreras, C., Burns, C. R., et al. 2017, *AJ*, 154, 211
- Kruckow, M. U., Tauris, T. M., Langer, N., Kramer, M., & Izzard, R. G. 2018, *MNRAS*, 481, 1908
- Kyutoku, K., Kiuchi, K., Sekiguchi, Y., Shibata, M., & Taniguchi, K. 2018, *PhRvD*, 97, 023009
- Leaman, J., Li, W., Chornock, R., & Filippenko, A. V. 2011, *MNRAS*, 412, 1419
- Levan, A. J., Lyman, J. D., Tanvir, N. R., et al. 2017, *ApJL*, 848, L28
- Li, W., Chornock, R., Leaman, J., et al. 2011, *MNRAS*, 412, 1473

- Linares, M., Shahbaz, T., & Casares, J. 2018, *ApJ*, 859, 54
- Lugaro, M., Campbell, S. W., Van Winckel, H., et al. 2015, *A&A*, 583, A77
- Lugaro, M., Ott, U., & Kereszturi, Á. 2018, *PtPNP*, 102, 1
- Macias, P., & Ramirez-Ruiz, E. 2018, *ApJ*, 860, 89
- Maeder, A., Grebel, A. K., & Merriliod, J.-C. 1999, *A&A*, 346, 459
- Maeder, A., & Meynet, G. 2001, *A&A*, 373, 555
- Mannucci, F., Della Valle, M., Panagia, N., et al. 2005, *A&A*, 433, 807
- Maod, D., Mannucci, F., & Brandt, T. D. 2012, *MNRAS*, 426, 3282
- Maod, D., Mannucci, F., & Nelemans, G. 2014, *ARA&A*, 52, 107
- Maod, D., Sharon, K., & Gal-Yam, A. 2010, *ApJ*, 722, 1879
- Martayan, C., Frémat, Y., Hubert, A.-M., et al. 2007, *A&A*, 462, 683
- Martin, D., Perego, A., Arcones, A., et al. 2015, *ApJ*, 813, 2
- Martin, D., Perego, A., Kastaun, W., & Arcones, A. 2018, *CQGra*, 35, 034001
- Mashonkina, L., Christlieb, N., & Eriksson, K. 2014, *A&A*, 569, A43
- Matteucci, F. 2014, *The Origin of the Galaxy and Local Group* (Berlin: Springer), 145
- Matteucci, F., & Greggio, L. 1986, *A&A*, 154, 279
- Matteucci, F., Romano, D., Arcones, A., Korobkin, O., & Rosswog, S. 2014, *MNRAS*, 438, 2177
- Matteucci, F., Spitoni, E., Recchi, S., & Valiante, R. 2009, *A&A*, 501, 531
- Mendoza-Temis, J. d. J., Wu, M.-R., Langanke, K., et al. 2015, *PhRvC*, 92, 055805
- Metzger, B. D., Bauswein, A., Goriely, S., & Kasen, D. 2015, *MNRAS*, 446, 1115
- Metzger, B. D., Thompson, T. A., & Quataert, E. 2007, *ApJ*, 659, 561
- Metzger, B. D., Thompson, T. A., & Quataert, E. 2008, *ApJ*, 676, 1130
- Mishenina, T., Pignatari, M., Carraro, G., et al. 2015, *MNRAS*, 446, 3651
- Mishenina, T., Pignatari, M., Côté, B., et al. 2017, *MNRAS*, 469, 4378
- Miyaji, S., Nomoto, K., Yokoi, K., & Sugimoto, D. 1980, *PASJ*, 32, 303
- Moffett, A. J., Ingarfield, S. A., Driver, S. P., et al. 2016, *MNRAS*, 457, 1308
- Montes, F., Beers, T. C., Cowan, J., et al. 2007, *ApJ*, 671, 1685
- Mösta, P., Roberts, L. F., Halevi, G., et al. 2017, *ApJ*, 864, 171
- Mumpower, M. R., Surman, R., McLaughlin, G. C., & Aprahamian, A. 2016, *PtPNP*, 86, 86
- Naiman, J. P., Pillepich, A., Springel, V., et al. 2018, *MNRAS*, 477, 1206
- Nishimura, N., Sawai, H., Takiwaki, T., Yamada, S., & Thielemann, F.-K. 2017, *ApJL*, 836, L21
- Nishimura, N., Takiwaki, T., & Thielemann, F.-K. 2015, *ApJ*, 810, 109
- Nishimura, S., Kotake, K., Hashimoto, M.-a., et al. 2006, *ApJ*, 642, 410
- Nomoto, K., Kobayashi, C., & Tominaga, N. 2013, *ARA&A*, 51, 457
- Nomoto, K., & Kondo, Y. 1991, *ApJL*, 367, L19
- Obergaulinger, M., & Aloy, M. Á. 2017, *MNRAS*, 469, L43
- Obergaulinger, M., Cerdá-Durán, P., Müller, E., & Aloy, M. A. 2009, *A&A*, 498, 241
- Palenzuela, C., Liebling, S. L., Neilsen, D., et al. 2015, *PhRvD*, 92, 044045
- Palmese, A., Hartley, W., Tarsitano, F., et al. 2017, *ApJL*, 849, L34
- Pan, Y.-C., Kilpatrick, C. D., Simon, J. D., et al. 2017, *ApJL*, 848, L30
- Papish, O., Soker, N., & Bukay, I. 2015, *MNRAS*, 449, 288
- Perego, A., Rosswog, S., Cabezón, R. M., et al. 2014, *MNRAS*, 443, 3134
- Perrett, K., Sullivan, M., Conley, A., et al. 2012, *AJ*, 144, 59
- Pian, E., D'Avanzo, P., Benetti, S., et al. 2017, *Natur*, 551, 67
- Pignatari, M., Gallino, R., Meynet, G., et al. 2008, *ApJL*, 687, L95
- Placco, V. M., Holmbeck, E. M., Frebel, A., et al. 2017, *ApJ*, 844, 18
- Podsiadlowski, P., Langer, N., Poelarends, A. J. T., et al. 2004, *ApJ*, 612, 1044
- Prantzos, N. 2008, in *EAS Publications Ser. 32*, ed. C. Charbonnel & J.-P. Zahn (Paris: EDP Sciences), 311
- Radice, D., Galeazzi, F., Lippuner, J., et al. 2016, *MNRAS*, 460, 3255
- Ritter, C., Côté, B., Herwig, F., Navarro, J. F., & Fryer, C. L. 2018a, *ApJS*, 237, 42
- Ritter, C., Herwig, F., Jones, S., et al. 2018b, *MNRAS*, 480, 538
- Roberts, L. F., Kasen, D., Lee, W. H., & Ramirez-Ruiz, E. 2011, *ApJL*, 736, L21
- Roberts, L. F., Lippuner, J., Duez, M. D., et al. 2017, *MNRAS*, 464, 3907
- Roberts, L. F., Woosley, S. E., & Hoffman, R. D. 2010, *ApJ*, 722, 954
- Roederer, I. U., Cowan, J. J., Karakas, A. I., et al. 2010, *ApJ*, 724, 975
- Roederer, I. U., Cowan, J. J., Preston, G. W., et al. 2014a, *MNRAS*, 445, 2970
- Roederer, I. U., Jacobson, H. R., Thanathibodee, T., Frebel, A., & Toller, E. 2014b, *ApJ*, 797, 69
- Roederer, I. U., Karakas, A. I., Pignatari, M., & Herwig, F. 2016a, *ApJ*, 821, 37
- Roederer, I. U., Kratz, K.-L., Frebel, A., et al. 2009, *ApJ*, 698, 1963
- Roederer, I. U., & Lawler, J. E. 2012, *ApJ*, 750, 76
- Roederer, I. U., Lawler, J. E., Cowan, J. J., et al. 2012a, *ApJL*, 747, L8
- Roederer, I. U., Lawler, J. E., Sobeck, J. S., et al. 2012b, *ApJS*, 203, 27
- Roederer, I. U., Mateo, M., Bailey, J. I., III, et al. 2016b, *AJ*, 151, 82
- Rosswog, S. 2015, *IJMPD*, 24, 1530012
- Rosswog, S., Feindt, U., Korobkin, O., et al. 2017a, *CQGra*, 34, 104001
- Rosswog, S., Korobkin, O., Arcones, A., Thielemann, F.-K., & Piran, T. 2014, *MNRAS*, 439, 744
- Rosswog, S., Liebendörfer, M., Thielemann, F.-K., et al. 1999, *A&A*, 341, 499
- Rosswog, S., Piran, T., & Nakar, E. 2013, *MNRAS*, 430, 2585
- Rosswog, S., Sollerman, J., Feindt, U., et al. 2017b, arXiv:1710.05445
- Rosswog, S., Sollerman, J., Feindt, U., et al. 2018, *A&A*, 615, A132
- Ruiter, A. J., Belczynski, K., & Fryer, C. 2009, *ApJ*, 699, 2026
- Ruiter, A. J., Ferrario, L., Belczynski, K., et al. 2018, *MNRAS*, 484, 698
- Safarzadeh, M., & Côté, B. 2017, *MNRAS*, 471, 4488
- Safarzadeh, M., Sarmento, R., & Scannapieco, E. 2018, arXiv:1812.02779
- Safarzadeh, M., & Scannapieco, E. 2017, *MNRAS*, 471, 2088
- Sakari, C. M., Placco, V. M., Hansen, T., et al. 2018, *ApJL*, 854, L20
- Sako, M., Bassett, B., Becker, A. C., et al. 2014, arXiv:1401.3317
- Schatz, H., Toenjes, R., Pfeiffer, B., et al. 2002, *ApJ*, 579, 626
- Schönrich, R., & Weinberg, D. H. 2019, arXiv:1901.09938
- Sekiguchi, Y., Kiuchi, K., Kyutoku, K., & Shibata, M. 2015, *PhRvD*, 91, 064059
- Shen, S., Cooke, R. J., Ramirez-Ruiz, E., et al. 2015, *ApJ*, 807, 115
- Siegel, D. M., Barnes, J., & Metzger, B. D. 2018, arXiv:1810.00098
- Siegel, D. M., & Metzger, B. D. 2017, *PhRvL*, 119, 231102
- Siegel, D. M., & Metzger, B. D. 2018, *ApJ*, 858, 52
- Simmerer, J., Sneden, C., Cowan, J. J., et al. 2004, *ApJ*, 617, 1091
- Simonetti, P., Matteucci, F., Greggio, L., & Cescutti, G. 2019, arXiv:1901.02732
- Siqueira Mello, C., Spite, M., Barbuy, B., et al. 2013, *A&A*, 550, A122
- Sneden, C., Cowan, J. J., & Gallino, R. 2008, *ARA&A*, 46, 241
- Sneden, C., Cowan, J. J., Lawler, J. E., et al. 2003, *ApJ*, 591, 936
- Soker, N., & Gilkis, A. 2017, *ApJ*, 851, 95
- Somerville, R. S., & Davé, R. 2015, *ARA&A*, 53, 51
- Spina, L., Meléndez, J., Karakas, A. I., et al. 2018, *MNRAS*, 474, 2580
- Spite, F., Spite, M., Barbuy, B., et al. 2018, *A&A*, 611, A30
- Stovall, K., Freire, P. C. C., Chatterjee, S., et al. 2018, *ApJL*, 854, L22
- Tanaka, M., Utsumi, Y., Mazzali, P. A., et al. 2017, *PASJ*, 69, 102
- Tanvir, N. R., Levan, A. J., González-Fernández, C., et al. 2017, *ApJL*, 848, L27
- Tauris, T. M., Kramer, M., Freire, P. C. C., et al. 2017, *ApJ*, 846, 170
- Thanjavur, K., Simard, L., Bluck, A. F. L., & Mendel, T. 2016, *MNRAS*, 459, 44
- Thielemann, F.-K., Eichler, M., Panov, I. V., & Wehmeyer, B. 2017, *ARNPS*, 67, 253
- Thompson, T. A. 2003, *ApJL*, 585, L33
- Thompson, T. A., & ud-Doula, A. 2018, *MNRAS*, 476, 5502
- Totani, T., Morokuma, T., Oda, T., Doi, M., & Yasuda, N. 2008, *PASJ*, 60, 1327
- Uddin, S. A., Mould, J., & Wang, L. 2017, *ApJ*, 850, 135
- van de Sande, J., Scott, N., Bland-Hawthorn, J., et al. 2018, *NatAs*, 2, 483
- van de Voort, F., Quataert, E., Hopkins, P. F., Kereš, D., & Faucher-Giguère, C.-A. 2015, *MNRAS*, 447, 140
- Van Der Walt, S., Colbert, S. C., & Varoquaux, G. 2011, *CSE*, 13, 22
- Vigna-Gómez, A., Neijssel, C. J., Stevenson, S., et al. 2018, *MNRAS*, 481, 4009
- Villar, V. A., Guillochon, J., Berger, E., et al. 2017, *ApJL*, 851, L21
- Vlasov, A. D., Metzger, B. D., & Thompson, T. A. 2014, *MNRAS*, 444, 3537
- Wallner, A., Faermann, T., Feige, J., et al. 2015, *NatCo*, 6, 5956
- Wanajo, S. 2018, *ApJ*, 868, 65
- Wanajo, S., Sekiguchi, Y., Nishimura, N., et al. 2014, *ApJL*, 789, L39
- Wang, H., Zhang, F.-W., Wang, Y.-Z., et al. 2017, *ApJ*, 851, 18
- Wehmeyer, B., Pignatari, M., & Thielemann, F.-K. 2015, *MNRAS*, 452, 1970
- Winteler, C., Käppeli, R., Perego, A., et al. 2012, *ApJL*, 750, L22
- Wollaeger, R. T., Korobkin, O., Fontes, C. J., et al. 2018, *MNRAS*, 478, 3298
- Woodward, P. R., Herwig, F., & Lin, P.-H. 2015, *ApJ*, 798, 49
- Woosley, S. E., Heger, A., & Weaver, T. A. 2002, *RvMP*, 74, 1015
- Wu, M.-R., Barnes, J., Martínez-Pinedo, G., & Metzger, B. D. 2018, *PhRvL*, 122, 062701
- Wu, M.-R., Fernández, R., Martínez-Pinedo, G., & Metzger, B. D. 2016, *MNRAS*, 463, 2323
- Zemp, M., Ramirez-Ruiz, E., & Diemand, J. 2009, *ApJL*, 705, L186
- Zhu, Y., Wollaeger, R. T., Vassh, N., et al. 2018, *ApJ*, 863, 23